

Paleoseismology of the Mejillones Fault, northern Chile: Insights from cosmogenic 10Be and optically stimulated luminescence determinations

J. Cortés A., Gabriel González L., S. A. Binnie, R. Robinson, S. P. H. T. Freeman, G. Vargas E.

▶ **To cite this version:**

J. Cortés A., Gabriel González L., S. A. Binnie, R. Robinson, S. P. H. T. Freeman, et al.. Paleoseismology of the Mejillones Fault, northern Chile: Insights from cosmogenic 10Be and optically stimulated luminescence determinations. Tectonics, 2012, 31, 10.1029/2011TC002877 . insu-03620304

HAL Id: insu-03620304
https://insu.hal.science/insu-03620304

Submitted on 26 Mar 2022

HAL is a multi-disciplinary open access archive for the deposit and dissemination of scientific research documents, whether they are published or not. The documents may come from teaching and research institutions in France or abroad, or from public or private research centers.

L'archive ouverte pluridisciplinaire **HAL**, est destinée au dépôt et à la diffusion de documents scientifiques de niveau recherche, publiés ou non, émanant des établissements d'enseignement et de recherche français ou étrangers, des laboratoires publics ou privés.

Copyright

Paleoseismology of the Mejillones Fault, northern Chile: Insights from cosmogenic ^{10}Be and optically stimulated luminescence determinations

J. Cortés A.,[1,2] Gabriel González L.,[1] S. A. Binnie,[3,4] R. Robinson,[5] S. P. H. T. Freeman,[6] and G. Vargas E.[7]

Received 24 January 2011; revised 1 March 2012; accepted 6 March 2012; published 26 April 2012.

[1] We have undertaken the first paleoseismological study on an upper plate fault in Chile. The selected structure was the Mejillones Fault, which is marked by a conspicuous fault-scarp. Using cosmogenic ^{10}Be and OSL dating and detailed sedimentary logging of trenches, we have constrained the abandonment of two alluvial surfaces by fault activity at ca. 35 ka and ca.14 ka. Based on stratigraphic observation we characterized the fault evolution in four intervals over the last ca. 35 ka. During the first three intervals the fault had a steady slip rate of 0.61 $\pm$ 0.26 m/ka. The fourth interval is delineated by the last vertical fault slip and the accumulation of un-deformed hillslope deposits after ca. 3.3 ka and has a slip rate of 0.22 $\pm$ 0.06 m/ka. The younger surface abandonment was caused by two Mw $\sim$ 7 paleoearthquakes with a recurrence interval of 5.0 $\pm$ 3.5 ka. The third interval is characterized by the interaction of hillslope deposits and aseismic slip and/or centimeter scale seismic slip events. At ca. 3.5 ka, a last large (Mw $\sim$ 6.6) earthquake took place. The recurrence intervals of large (Mw > 8.5) subduction earthquakes do not appear to be the same as the recurrence intervals of the Mw $\sim$ 7 events on the upper plate Mejillones Fault.

Citation: Cortés A., J., G. González L., S. A. Binnie, R. Robinson, S. P. H. T. Freeman, and G. Vargas E. (2012), Paleoseismology of the Mejillones Fault, northern Chile: Insights from cosmogenic ^{10}Be and optically stimulated luminescence determinations, *Tectonics*, *31*, TC2017, doi:10.1029/2011TC002877.

1. Introduction

[2] The subduction of oceanic crust below the South American Plate is the first order control on bulk strain accumulation in the overriding plate, making the coastal region of northern Chile one of the most important seismically active zones in the Circum-Pacific area [*Nishenko*, 1991; *Delouis et al.*, 1997, 2009; *Comte et al.*, 1999]. Several geophysical and geodetic groups have studied the seismic cycle of large subduction earthquakes along this margin, demonstrating that, over the short-term, slip deficit produces significant elastic (non-permanent) deformation in the upper plate at the plate boundary [*Bevis et al.*, 1999; *Klotz et al.*, 2001; *Chlieh et al.*, 2004; *Klotz et al.*, 2006]. This implies that the present-day deformation is exclusively elastic and that permanent deformation is not occurring in the upper plate overlying the seismogenic zone. However, evidence of permanent deformation (inelastic strain), expressed as kilometer-long faults affecting Quaternary deposits [*Armijo and Thiele*, 1990; *Delouis et al.*, 1998, *González et al.*, 2003; *Allmendinger et al.*, 2005, *Allmendinger and González*, 2010], suggests the opposite. Resolving this dichotomy requires more information on two key aspects of active faulting in northern Chile, namely the age of the most recent displacements, and how much deformation is absorbed along these faults through time. Passive seismic experiments have not identified shallow seismicity in upper plate faults [*Arabasz*, 1971; *Comte et al.*, 1992]. This, coupled with our poor understanding of basic paleoseismic data, such as slip-rate, earthquake paleomagnitudes and recurrence times, has obscured the linkage between large earthquakes, upper plate faults and the determination of seismic hazards associated with them.

[3] In this contribution we undertake a paleoseismological study of the Mejillones Fault, one of the most significant faults of the coastal region in northern Chile. This fault is exposed in the eastern part of the Mejillones Peninsula (Figures 1a and 1b), where it is expressed as a conspicuous fault scarp preserved in alluvial fan deposits (Figure 2). This fault separates the uplifted Mejillones Horst to the west from

[1]Departamento de Ciencias Geológicas, Universidad Católica del Norte, Antofagasta, Chile.
[2]Géosciences Environnement Toulouse, Université Paul Sabatier, Toulouse, France.
[3]Institute of Geography, University of Edinburgh, Edinburgh, UK.
[4]Now at Institut für Geologie und Mineralogie, Universität zu Köln, Cologne, Germany.
[5]Department of Earth Sciences, University of St Andrews, St Andrews, UK.
[6]Scottish Universities Environmental Research Centre, East Kilbride, UK.
[7]Departamento de Geología, Facultad de Ciencias Físicas y Matemáticas, Universidad de Chile, Santiago, Chile.

Copyright 2012 by the American Geophysical Union.
0278-7407/12/2011TC002877

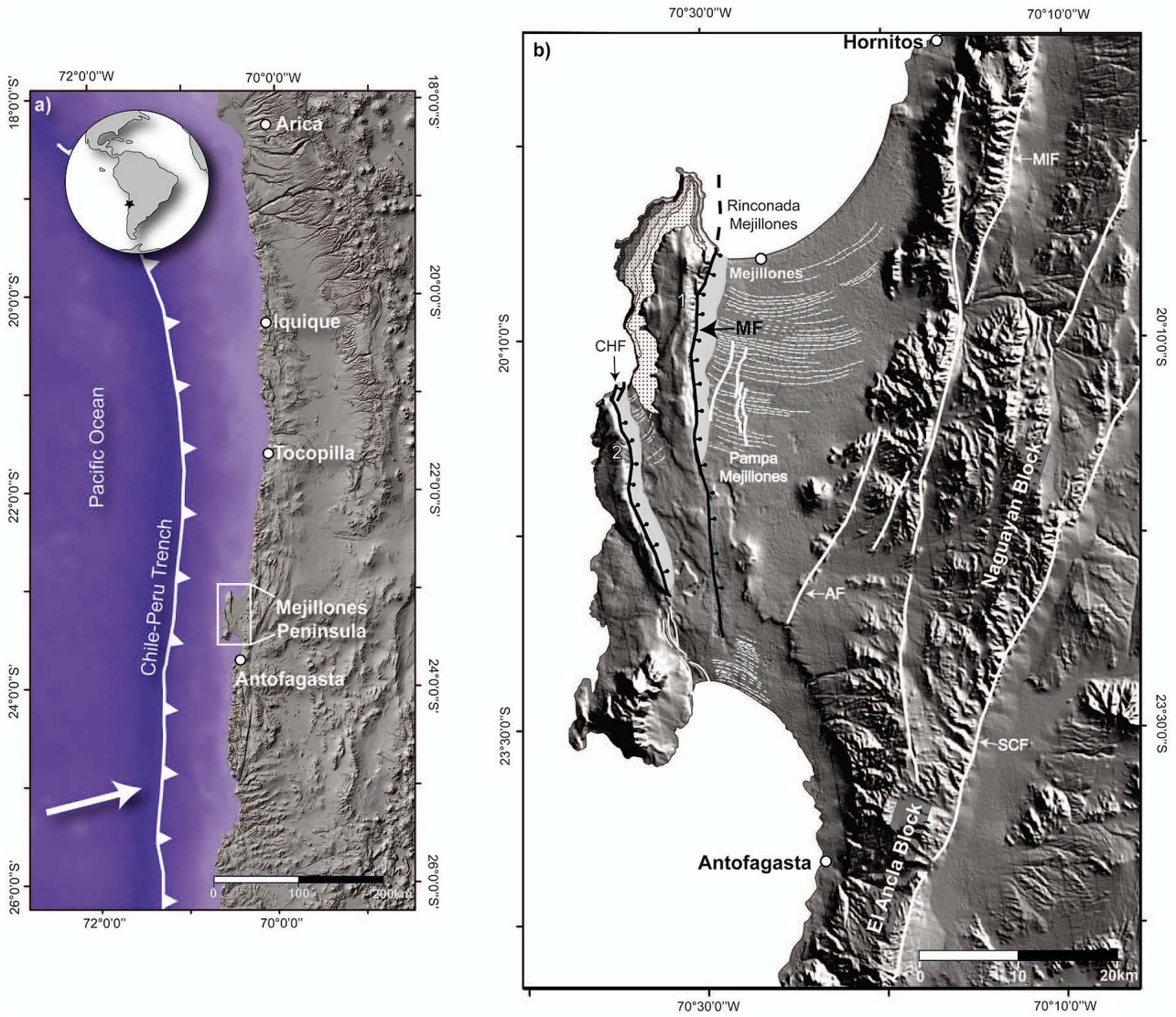


Figure 1. (a) Shaded relief map of northern Chile made from SRTM 90 data. The Mejillones Peninsula is bordered by a white rectangle. The white arrow represents the convergence at 65 mm/ y and oriented ~75E [*Angermann et al.*, 1999]. (b) Shaded relief map of the Mejillones Peninsula elaborated by using SRTM 90 data. The numbers 1 and 2 indicate the Mejillones and Jorgino horst, respectively. Dotted polygons represent uplifted marine terraces of Middle-Late Pleistocene age. White segmented lines in Pampa Mejillones are paleobeach ridges. Black lines in the Mejillones Peninsula and white lines further east are normal faults in the locality. The Mejillones Fault scarp is represented by small tick marks.

the Pampa Mejillones to the east (Figure 1b). Despite the strong morphological expression of the Mejillones Fault, no historical seismicity has been reported on it. Here, we determined the displacement-earthquake history for the last ca. 14 ka, estimating the magnitude of past earthquakes and their average recurrence interval using detailed trench logging, cosmogenic ^{10}Be exposure ages and optically stimulated luminescence (OSL) dating. We compare our findings to those of a previous study that used cosmogenic ^{10}Be to constrain the abandonment ages of the alluvial surfaces [*Marquardt*, 2005], and present new data to clarify the significance of the surface exposure ages and their relationship with the recent activity of the Mejillones Fault.

2. Seismo-Tectonic Setting and Upper Plate Fault Context

[4] The tectonics of northern Chile is dominated by the convergence between the Nazca and South American plates. Currently, the convergence is approximately orthogonal to the margin (~75°E) [*Angermann et al.*, 1999] and is taking place at a velocity of ~65 mm/yr [*Angermann et al.*, 1999]. Upper plate faults of the coastal area in northern Chile are

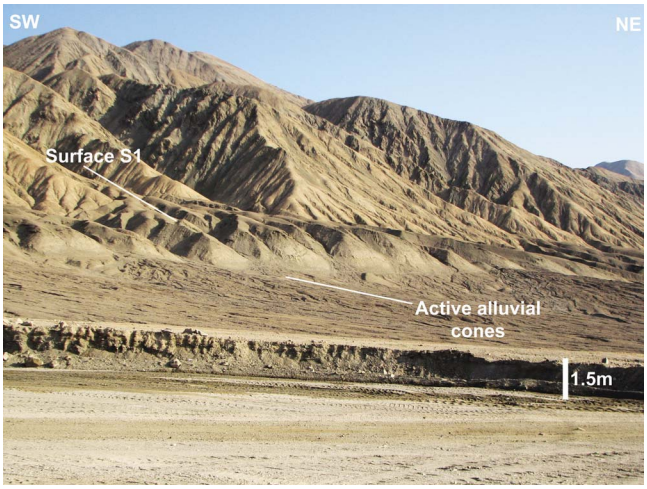


Figure 2. Northwestern view of the Mejillones Fault Scarp, uppermost surface of the alluvial fan is the Surface S1. Note the active alluvial cones accumulated at the foot of the scarp.

located above the seismogenic zone of the Central Andes. The extension of the seismogenic zone has been addressed using teleseismic data [*Tichelaar and Ruff*, 1991] and local networks [*Husen et al.*, 1999; *Delouis et al.*, 1996; *Comte et al.*, 1994]. The location of the 1995 Mw 8.1 Antofagasta and 2007 Mw 7.7 Tocopilla subduction earthquakes, and their aftershocks, has revealed the downdip extension of the seismogenic zone to be at 50 ± 5 km depth [*Husen et al.*, 1999, 2000; *Buske et al.*, 2002].

[5] Upper plate faults in the coastal region near Antofagasta and the Mejillones Peninsula are oriented parallel to the trench. The most prominent upper plate fault in the area, the Salar del Carmen Fault (SCF in Figure 1b), forms part of the main trace of the Atacama Fault Zone. This structure is situated in the western border of the Sierra el Ancla and Sierra Naguayan blocks, forming a 300 m high vertical step in the topography (Figure 1b). Other relevant structures in this area are the Mejillones Fault and the Caleta Herradura Fault (MF and CHF in Figure 1b). These normal faults dissect the Mejillones Peninsula and control the topography of the half-grabens that characterize this morphological feature. The most recent fault activity in this area is expressed by the vertical offset of Quaternary alluvial and marine deposits. These faults form prominent fault scarps that were recognized during the seventies by *Arabasz* [1971] and *Okada* [1971].

[6] The kinematics of the upper plate faults is controversial. Several works have reported normal and sinistral faulting along these structures [*Armijo and Thiele*, 1990; *Niemeyer et al.*, 1996; *Delouis et al.*, 1998; *González et al.*, 2003]. Furthermore, along the inner part of the Coastal Cordillera between Iquique and Paposo, *Carrizo et al.* [2008] and *Allmendinger and González* [2010] documented trench parallel reverse faults. Geological observations (e.g., normal faults affecting reverse fault and vice versa) suggest that periods of E-W extension have alternated with periods of E-W shortening. The predominant horst and graben topography in the Mejillones Peninsula indicates that extension is currently the dominant process in the upper plate. Despite the occurrence of reverse faults, our structural and morphological observations in the area of Mejillones indicate that the net deformation expressed in the landscape is extensional, and that it has occurred since the Miocene [*Niemeyer et al.*, 1996; *Allmendinger and González*, 2010].

[7] Some mechanisms that have been postulated to explain extension along the normal faults in the upper plate are (1) subduction erosion [e.g., *Armijo and Thiele*, 1990; *Niemeyer et al.*, 1996], (2) coseismic elastic rebound of the upper plate during subduction earthquakes [*Delouis et al.*, 1998], and (3) upper plate bending during the interseismic period of subduction earthquake cycle [*Delouis et al.*, 1998; *González et al.*, 2003; *Loveless et al.*, 2005]. Despite these theories, the relationships between the phases of the subduction-earthquake cycle and upper plate fault activity are still a matter of debate, and not well understood. However, during the postseismic phase of the 2010 Mw 8.8 Maule earthquake in southern Chile, several shallow crustal events with normal focal mechanisms occurred in the area of the Pichilemu Fault (http://www.globalcmt.org; ID:201003111439A). The main shock was a Mw 6.9 one, which was followed by other subcrustal earthquakes that were concentrated at the base of the Pichilemu Fault (31.20°S) [*Comte et al.*, 2010], indicating that the entire fault was seismically reactivated. This is the first evidence for upper plate normal faulting in the Chilean margin being caused by large subduction earthquakes. It poses the question as to whether the activity of normal faulting is a result of coseismic elastic rebound caused by large subduction earthquakes. In a later section we will discuss this possibility for the Mejillones Fault.

3. Morphotectonics of the Mejillones Peninsula

[8] The Mejillones Peninsula is an anvil-shaped promontory jutting conspicuously from the typically north-south linear coastline of northern Chile (Figures 1a and 1b). The occurrence of Pliocene and Pleistocene marine abrasion platforms indicates that this peninsula has uplifted over the last ~3.8 my [*Marquardt*, 2005]. Marine terrace abandonment during the last 400 ka is associated with normal slip along the Mejillones Fault and Caleta Herradura Fault and uplift of the Mejillones Peninsula [*Marquardt*, 2005; *Victor et al.*, 2011]. These faults dip 60–70° to the east [*González et al.*, 2003] (Figure 1b) and produce cumulative vertical offsets of as much as 700 m [*Allmendinger and González*, 2010]. The Caleta Herradura Fault generates a rollover anticline in the hanging wall, which has previously been interpreted as reflecting a listric geometry at depth, with detachment levels at depths between 2000 m [*Allmendinger and González*, 2010] and 3750 m [*Pelz*, 2000]. The Mejillones and Caleta Herradura faults are related to the existence of two topographic highs, the Mejillones Horst (1) and Jorgino Horst (2), both depicted in Figure 1b. These horsts are made of Paleozoic granodioritic and metamorphic rocks. Approximately 500 m of cumulative vertical offset along the normal faults is expressed in the topography of the horst and graben structures [*Armijo and Thiele*, 1990; *González et al.*, 2003]. Miocene-Pleistocene marine sediments fill two half-graben, which lie eastward of the Caleta Herradura (CHF) and Mejillones (MF) faults (Figure 1b). Uplifted marine terraces of Middle-Late Pleistocene age (Figure 1b) are preserved along the flank of the horsts in a staircase pattern [*Armijo and Thiele*, 1990; *González et al.*, 2003]. The Pampa Mejillones is a planar surface lying east of the Mejillones

Fault (Figure 1b), and is composed of Pliocene marine sediments overlain by Quaternary marine deposits. *Marquardt* [2005] assigned these marine terraces to the maximal Late Pleistocene interglacial highstands [*Shackleton et al.*, 1990], beginning with MIS 11. Symmetrical and semicircular patterns of paleobeach ridges are present in the northern and southern extents of the Pampa Mejillones (Figure 1b). Other uplifted regions include the marine abrasion platform of Antofagasta city, and the coastal portion from Mejillones to Hornitos beach (Figure 1b). Age determinations for these marine terraces and paleobeach deposits [*Ortlieb et al.*, 2003] indicate a 0.5–0.2 m/ka long-term uplift rate for the Mejillones Peninsula and surrounding areas. The age assignation of *Marquardt* [2005] suggests that, for the Pampa Mejillones, uplift started at least 400 ka ago. Based on this assumption, *Marquardt* [2005] estimated an uplift rate of 0.5 to 0.7 m/ka for the horst and 0.2–0.3 m/ka for the Pampa Mejillones, with the difference of 0.5 to 0.2 m/ka resulting from the slip rate of the Mejillones Fault.

4. The Mejillones Fault

[9] The Mejillones Fault is a 36 km long normal fault oriented north-south that extends from the southern part of the Mejillones Peninsula to the northern part of the Mejillones Pampa (Figure 1b). Offshore, *González et al.* [2009] used acoustic data to identify the seaward continuation of the Mejillones Fault for around 4 km, and the combined onshore and offshore lengths total 40 km. Fault plane exposure shows that the fault motion is dominated by east-side down slip (rake 80–70° down northward) along a fault plane orientated N10E/65E. The sinistral lateral component along this fault represents only a 17% of the along dip component of the slip. We concentrated our paleoseismological studies on the northernmost extension, covering 8 km of the fault trace. In this section, the fault exhibits two segments joined by a relay ramp structure. The northern section of the fault trace displays a continuous scarp along the entire trace of the Mejillones Fault. To the south, the fault has formed scarps in Quaternary alluvial and marine sediments, which generally have less vertical slip and are more discontinuous and degraded relative to the northern trace of the fault.

[10] The Mejillones Fault has experienced slip from at least the Miocene until the Quaternary [*Niemeyer et al.*, 1996]. The normal fault activity has accommodated the subsidence of the Mejillones Graben, allowing the accumulation of ~300 m of marine sediments since Pliocene-Pleistocene times. To the north, activity on the Mejillones Fault has formed a spectacular fault scarp (Figure 2), which offsets the Late Pleistocene-Holocene alluvial deposits [*Marquardt et al.*, 2004]. This scarp is well exposed for 8 km near the western periphery of the Mejillones Pampa (Figure 1b).

[11] Vertical slip on the Mejillones Fault during the Pleistocene promoted the formation of a broad piedmont from the eastern flank of the Mejillones Horst over the western extent of the Pampa Mejillones [*Marquardt*, 2005]. The piedmont contains alluvial fans and alluvial cones, forming growth strata in the hanging wall of the Mejillones Fault. This accumulation includes debris flow deposits that occurred during Pleistocene-Holocene torrential rain events [*Vargas et al.*, 2000, 2006].

4.1. Morphology of the Piedmont

[12] Along the northernmost part of the fault trace, on the piedmont of the Mejillones Horst, we identified four surfaces that are spatially and temporary related to the Mejillones Fault. Some of these surfaces were previously described and dated by *Marquardt* [2005]. As *Marquardt* [2005] did, we named these surfaces, from oldest to youngest, S1, S2, S3, and S4 (Figures 3a–3f). Surface S1 is best preserved along the footwall of the Mejillones Fault, presents an average slope inclination of 5°–6° to the east, and is clearly affected by the fault. Vertical offset of Surface S1 has generated the prominent scarp that characterizes the Mejillones Fault. Surface S2 corresponds to a younger alluvial surface cut into S1 and preserved locally on both sides of the Mejillones Fault. Surface S2 is found only at the mouth of the three large valleys that drain the Mejillones Horst (Figure 4). In the footwall, Surface S2 appears to have been formed by erosion of Surface S1. In the hanging wall, Surface S2 is inclined 12° to 19° to the east, whereas in the footwall block it generally has a lower dip. Surface S3 is an alluvial surface cut into S2 and is less extensive than S1 and S2, exhibiting a slope of 12° to 15° to the east at both sides of the fault. This surface is subtly offset by the fault. At one locality (23.116307°/70.495533°; Figures 3a and 8a), we observed a 15 cm high scarp and several centimeter wide fissures (tension cracks). Surface S4 corresponds to the youngest alluvial deposits in the study area and is preserved exclusively in the hanging wall. This surface is composed of the present-day active channel deposits and small alluvial cones close to the scarp (Figures 3a–3f). The alluvial cones are currently active, and are restricted to the mouth of gullies that drain the fan surfaces and cut the fault scarp. We observed decimeter-scale knickpoints in some of the channels, which have presumably retreated upstream from the fault plane. Alluvial cones formed at the channel mouths have very high slopes ~20° (Figures 5a–5c). Trenches dug through the cones show that the alluvium beneath Surface S4 is partially truncated by the fault.

[13] The formation of the S1 and S2 surfaces reflects the progressive accumulation of slip on the Mejillones Fault, and the alluvial fan/drainage system response to fault slip. The abandonment of Surface S1 and generation of Surface S2 may be due to one or several slip events on the fault, and/or an increased erosional capacity of the fluvial system. The spatial distribution of the surfaces relative to the fault trace suggests the former is most significant. In particular, Surface S2 exists exclusively where the three largest valleys dissect the Mejillones Fault scarp (Figure 4). Further south, where the scarp is almost absent, the piedmont is composed of a single alluvial surface with a dense network of deeply incised channels (Figure 6). We therefore suggest that the abandonment of alluvial surfaces in this area are closely related to the formation of the scarp, and hence to slip on the Mejillones Fault.

4.2. Characterization of the Mejillones Fault Scarp and Surface Offset

[14] We characterized the morphology of the Mejillones Fault scarp and the surface offset by performing 17 topographic profiles across it. These profiles and their locations are provided as auxiliary material.[1] Profiles were made with

[1]Auxiliary materials are available in the HTML. doi:10.1029/2011TC002877.

two differential GPS stations with a vertical accuracy of around 10 mm. We established the difference in position between two receptors (kinematic and static). The relative position of each receptor can be constrained with an accuracy of around 20 cm. In our profiles, the kinematic station recorded position (north, east, altitude) data every 3 s.

[15] In general, where Surface S1 is preserved in the footwall, we observe a characteristic geometry in the scarp profile expressed by a sharp break located in the middle part of the scarp (Figure 5a). This break separates a gentler slope in the uppermost part and a steeper slope in the lower part. The sharp break in the scarp slope is marked by the occurrence of

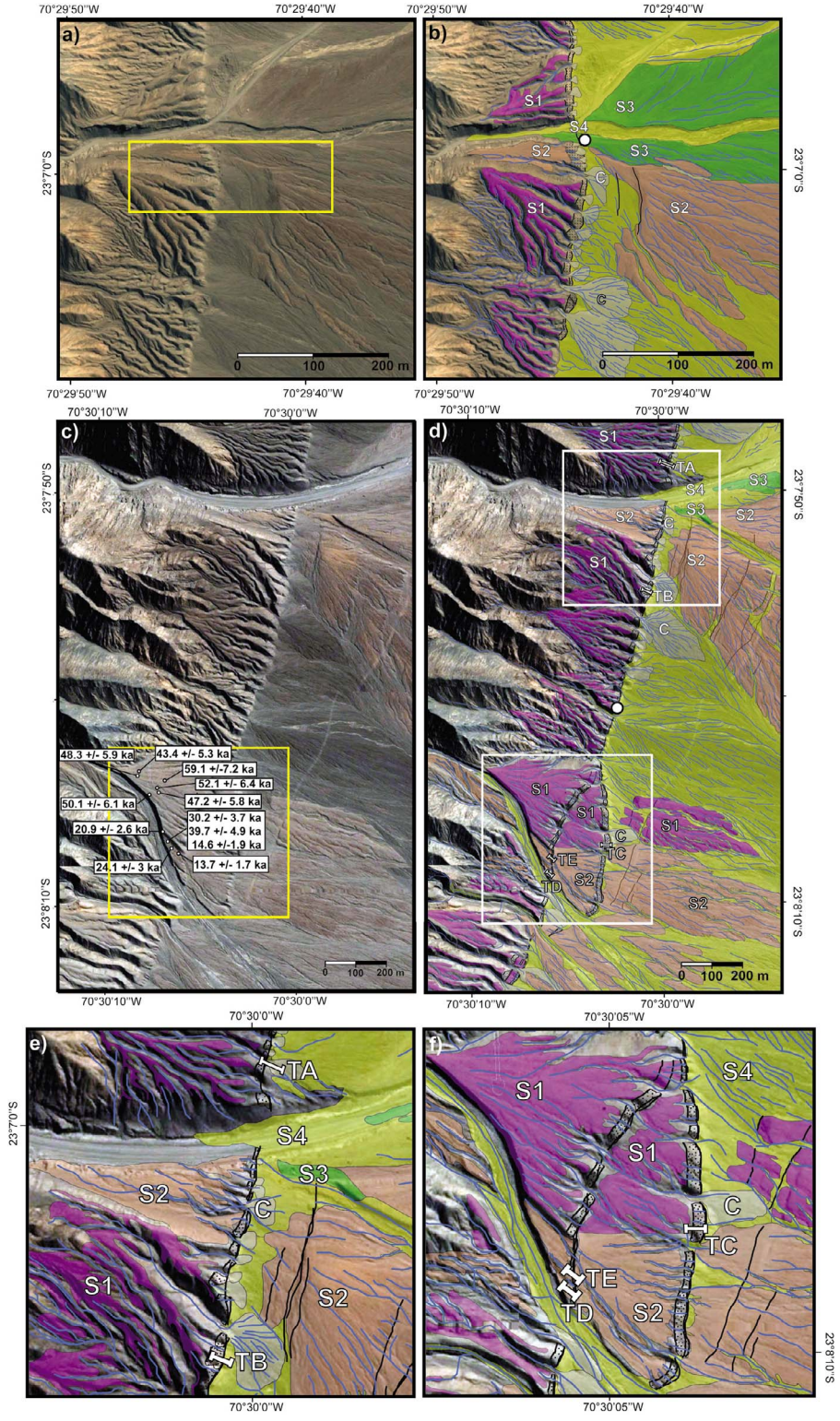


Figure 3

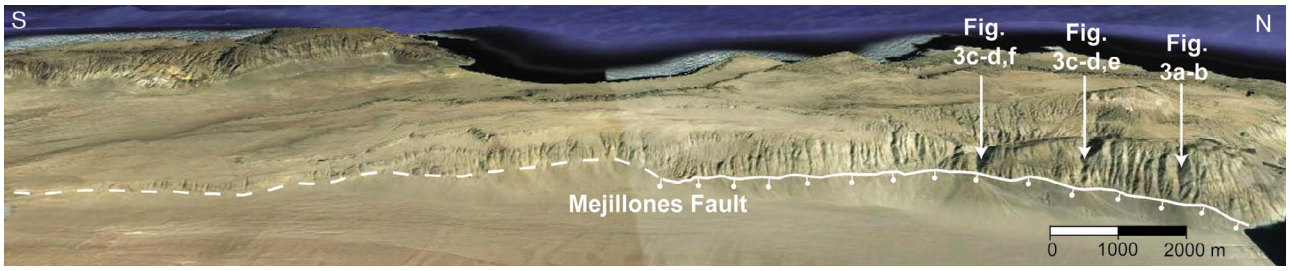


Figure 4. Oblique view of the Mejillones Fault scarp on Google Earth. White vertical lines depict the deepest and largest valleys, which cut across the western flank of the Mejillones Horst. The presence of S2 is restricted to the areas where these valleys drain. The white continuous line corresponds to the portion of the fault where the scarp is developed. The white segmented line indicates the fault segment where no scarp was present.

a free face. The portion of the scarp with the gentler slope generally constitutes the 50% to 40% of the entire scarp height (between the head and the base). In this part the dominant slope angle is 30°. The lower part is dominated by slope angles between 35° to 40°, indicating that the scarp profile angle is controlled by the debris slope angle. The higher slope (>45°) in the middle part of the scarp highlights the preservation of the free face (Figures 5a–5c). At the foot of the scarp the slope angle varies between 15° to 20° and corresponds to the wash slope.

[16] In the uppermost part of the scarp it is possible to see the occurrence of one to three additional slope-breaks (Figure 5a). *Wallace* [1977] proposed that in general breaks in slope represent discrete slip events on the underlying fault. Hence, the occurrence of such breaks of slope on the Mejillones Fault scarp suggests that their formation was due to more than one slip event occurring after the development of S1. However, breaks in the slope of a scarp can also be the result of local depositional events and/or strata more resistant to erosional processes [e.g., *McCalpin*, 1996]. By observing the topographic profiles, we noted that the breaks in the uppermost part of the scarp, between Surface S1 and Surface S2, are formed in alluvial gravels displaced by the fault. We observe that these gravels are lithologically similar along the fault trace and do not show evidence that suggests deposition or differential erosion. Therefore, we conclude that these breaks are tectonic imprints produced by scarp evolution at some time between S1 and S2 formation. Topographic characterization of the scarp indicates that the sharp break dividing its profile into upper and lower sections correlates in altitude with the Surface S2. Hence, we suggest that this major break represents a change in the scarp evolution and will discuss this further below in light of our age constraints.

[17] We estimated the surface offset from the topographic profiles by measuring the vertical distance between the tangent to the Surfaces S1 and S2 in the footwall, and the tangent to the Surface S4 in the hanging wall. Because we did not measure the vertical distance between the same surfaces, these data represent a minimum for the real surface offset. However, we observed in some locations that Surface S1 and S2 are close to the same topographic level as Surface S4. Therefore, surface offset can be considered as a good approximation to the cumulative vertical fault displacement since the beginning of the continental alluvial deposition. Where Surface S1 appears better preserved in the footwall block, the offset is larger and about 9.7 ± 5 m (the reported error represents the variation in the surface offset measurements, Figure 7). The surface offset of S1 increases northward from the southern tip of the fault. Where Surface S2 is displaced by the fault, the surface offset variation along strike of the fault is 3.8 ± 2.5 m. The greatest amount of surface offset of Surface S2 was also observed along the central part of the scarp (Figure 7). The variation of slip between surface offset of Surfaces S1 and S2 along strike of the scarp is 8.0 ± 6.7 m. In several locations along the Mejillones Fault we observed isolated small-scale fault scarps (~20 cm) in the debris slope (Figure 8a–8c). We found four of these scarps parallel to the larger main scarp. Vertical displacements across these structures vary between 10 and 30 cm. These fault scarps represent the latest visible displacement along the Mejillones Fault.

5. Trenches at the Mejillones Fault

[18] In order to characterize the paleoearthquake history of the Mejillones Fault we dug eight trenches across the

Figure 3. (a) Google Earth image of the site where *Marquardt* [2005] collected samples for ^{10}Be analysis. The yellow rectangle limits the sampling area. (b) Geomorphological map of the alluvial surfaces (S1, S2, S3, S4 and C) at site showed in (Figure 3a. (c) Google Earth image of the Mejillones Fault where we dug trenches and collected samples for ^{10}Be analysis. White circles depict each sample site. Marquardt's sampling site is also represented by a yellow rectangle. (d) Geomorphological map of the alluvial surfaces (S1, S2, S3, S4 and C) at site shown in C. Trenches are indicated by white bracketed lines and the labels TA, TB, TC and TD. White rectangles correspond to subsets shown in Figures 3e and 3f. (e) Close-up of the sites where TA and TB were excavated. (f) Close-up of the sites where TC, TD and TE were dug. In all the geomorphological maps a black doted zone limited by black lines represents the scarp. Black lines farther east are lineaments, probably corresponding to normal faults. Blue lines are drainages present in the study area.

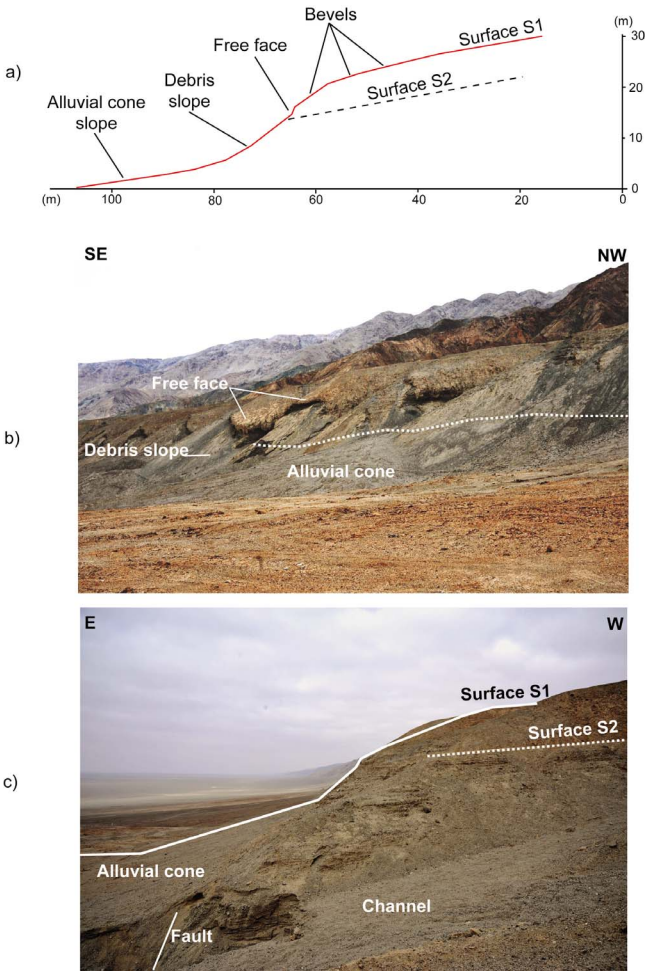


Figure 5. (a) Topographic profile at TB site. The different parts of the scarp are indicated and the breaks in the slope highlighted. The black segmented line represents the position of Surface S2. The high slope of the alluvial cones can be observed at the base of the profile. (b) View of the scarp at trench B site. Free face and debris slope are indicated. White dotted line represents the position of the Mejillones Fault. The steep slopes of the alluvial cones can be observed. (c) Profile view of the Mejillones Fault scarp. White segmented line indicates the position of Surface S2 in the scarp profile.

scarp, and selected five trenches for mapping (labeled as A, B, C, D and E; see trench location in Figures 3d–3f). We consider two types of morphological sites for trenching; one to expose the fault-scarp and the other to expose the alluvial cones formed where gullies erode the scarp. The former (B, C and D) exposes the sediments accumulated at the base of the scarp, including the debris slope and the wash slope. The latter (A and E) expose sediments transported by fluvial processes or sheetflow and deposited eastward of the scarp as alluvial cones. These two types of sites help shed light on fault scarp processes (mainly degradation and alluvial channel incision) in the presence and absence of channel systems, and the variability of sedimentary style. The deposits were sketched and sedimentary panels (2D logs) were recorded to provide a detailed investigation of the sedimentary responses to discrete slip events on the Mejillones Fault. The trenches were dug approximately 10 m long, 3 m wide and 2.5 m deep. In general, similar sedimentary architecture is exposed in the facing walls of the trenches.

[19] In the data repository we give a detailed description of the stratigraphy of each trench. Here, we summarize the most relevant stratigraphic data for the interpretation of the fault paleoseismology. We noted that the stratigraphy of the trenches consists, in general, of deformed alluvial gravels west of the fault and a group of sedimentary deposits formed on the east side of the fault in response to fault slip and scarp degradation. The alluvial deposits (unit AG1 in the 2D log panels of trench A, B and C; Figures 9, 10, and 11) consist of coarse-grained gravels that were accumulated in beds of 15 to 40 cm thickness. This unit (AG1) continues to the west beneath Surface S1 and corresponds to the fan material deposited prior to S1 formation, which was subsequently deformed by the Mejillones Fault. In trenches A, B, and C the alluvial gravels are similar in texture to the alluvial gravels exposed in trenches D and E. The main difference is that these gravels are localized beneath Surface S2 in trenches D and E (Figures 12 and 13), and thus they represent the material deposited prior to the formation of this surface.

[20] The sedimentary material accumulated eastward of the fault is a scarp-derived colluvium, which, following *Nelson* [1992], can be divided into a lower section of debris facies and an upper section of wash facies. The debris facies is made of clast-supported and massive gravels. In this facies we identified two colluvial wedges that are represented by CW1 and CW2 in the 2D log panels (Figures 9–13). The colluvial wedges are stratigraphically separated by an angular unconformity and an oxidized soil-horizon (Figures 10c, 11, and 12). Although the sedimentary materials composing units

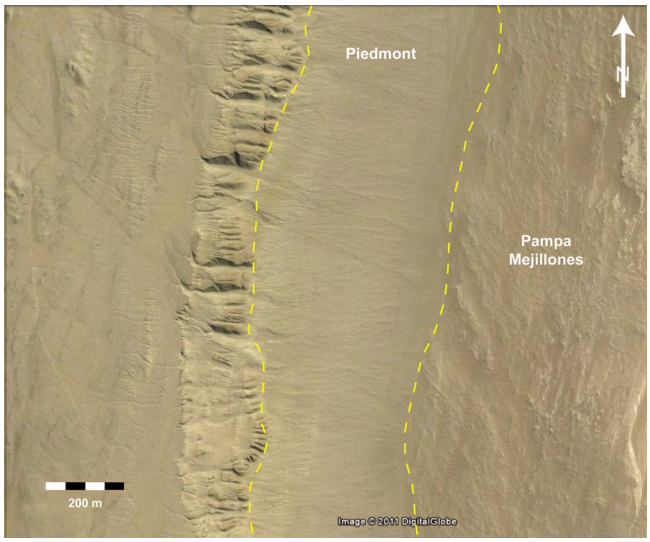


Figure 6. Google Earth image showing a portion of the southern segment of the Mejillones Fault. At this site the piedmont is constructed by a unique alluvial surface and there is no scarp present. Yellow segmented lines limit the extent of the piedmont.

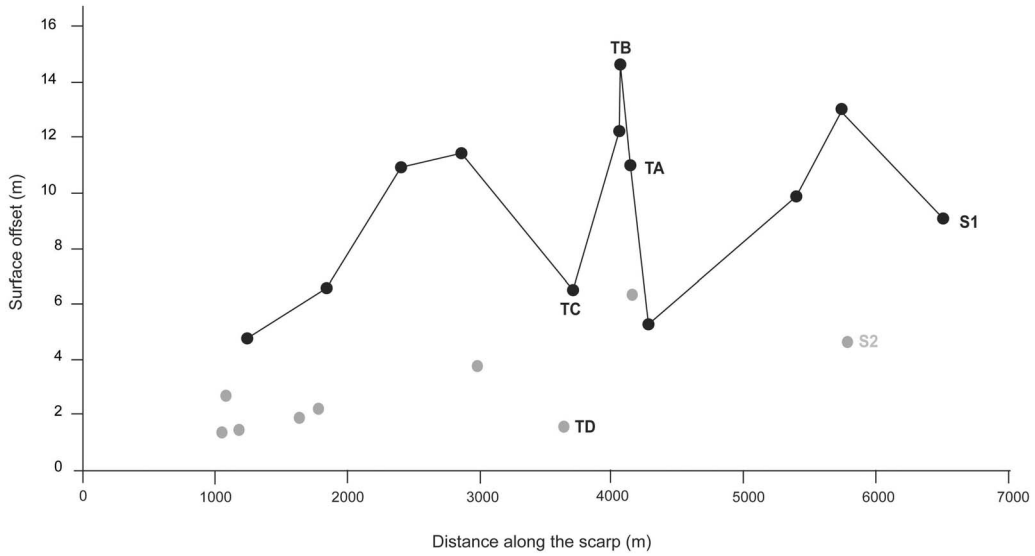


Figure 7. Shows the surface offset at both sites, where Surfaces S1 (black line) and S2 (gray dots) are preserved in the footwall block. Where Surface S1 is preserved, surface offset varies between 4.7 and 14.7 m, and where Surface S2 is preserved surface offset varies between 1.3 and 6.3 m.

CW1 and CW2 are derived from degradation of the unit AG1, both colluvial wedges differ in their sedimentary fabric with respect to the alluvial gravels in the footwall block (AG1). The alluvial gravels are clearly stratified with horizontal bedding (Figures 14a and 14c). In contrast, CW1 and CW2 have in general a chaotic appearance with no bedding. The thickness of these deposits decreases from the fault to the east, suggesting that they were formed suddenly when the free face of an earlier fault scarp was degraded. From trenches D and E we determined that these two colluvial wedges are related to the uplift of Surface S2.

[21] The colluvium forming the wash facies is distinctly finer grained, better sorted and stratified. It is composed of a succession of fine gravels interbedded with sandy horizons. In general, as we show in Figures 10b and 10c, the wash facies has an abrupt lower contact with the debris facies and exhibits a decreasing thickness tapering away from the fault plane. The interbedded fabric dips 30–35° and it is subparallel to the scarp slope (Figures 14a–14c). We identified that the fine gravels and sandy layers in these deposits do not have densely packed granular matrices (Figure 14b), suggesting that this wash facies was accumulated by successive gravitationally controlled grain flows. In general, this type of deposit forms after complete disappearance of the free face by diffusion; activated by rain splash, wind action and/or seismic shaking [*McCalpin*, 1996]. Considering the sedimentological characteristics of the wash facies and its transport mechanisms, we named this deposit collectively as hillslope deposit (HSD). We divide these hillslope deposits into HSD1 and HSD2. Because the Mejillones Fault cuts the HSD1, generating a notable difference in thickness between the hanging wall and footwall blocks (Figure 10b), we interpret the accumulation of this unit as being contemporaneous with downward slip along the Mejillones Fault. This is similar to growth strata associated with normal faulting.

[22] In trenches A, C and E we identified a colluvial wedge (CWD in trench A, Figure 9b, and CW3 in trenches C and E, Figures 11a–11c, 13b, and 13c) that overlies the hillslope deposit HSD1. The relationship between fault activity and the sedimentary record identified in all the trenches can be summarized as follows. In the northern segment, the colluvial wedges (CW1 and CW2) and the overlying hillslope deposit (HSD1) are affected by the fault. The third colluvial wedge (CWD-CW3) is deformed in trench A (Figure 9b), but is not affected by the fault in trench C (Figures 11a–11c). In all the trenches we observed that the fault does not deform the uppermost part of the trench stratigraphy (the last 40–100 cm corresponding to HSD2 and the alluvial gravel AG4 in trench A).

[23] In several locations along the Mejillones fault, small scarps of 10 to 30 cm in height and a few meters in length (Figure 8) have been formed and represent the most recent activity on the fault. Also, in some places we noted that the hillslope deposits bury the fault. These observations indicate that the most recent activity of the Mejillones Fault produced localized ruptures.

6. Estimates of Cumulative Displacement in the Trenches

[24] In order to derive the cumulative fault displacement that occurred after the abandonment of Surface S2, we used the exposed (minimal) thicknesses of the colluvial wedges and the hillslope deposits visible in our five trenches. *McCalpin* [1996] states that the maximum coseismic slip during an earthquake is limited to twice the thickness of the colluvial wedge that it generated. Because the colluvial wedges that we documented in the trenches suffered some erosion after deposition, our magnitude of slip has to be considered as a minimum. We measured minimal thicknesses of 1.5 m, 0.7 m and 0.7 m for CW1 in trenches B, C

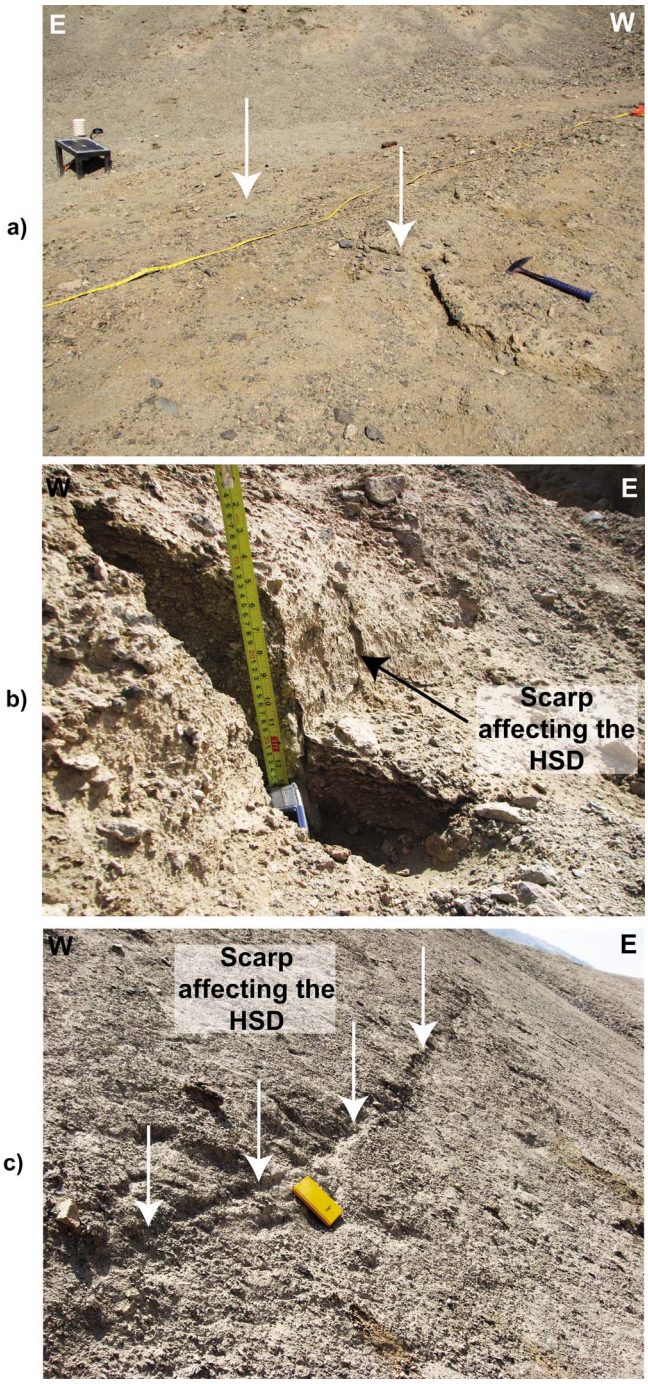


Figure 8. (a) Subtle scarp developed in a site where the Mejillones Fault affects Surface S3 (23.116307°/70.495533°; Figure 3a). The hammer is laid on the scarp and the yellow tape measure is located across the scarp marking the subtle vertical displacement. (b) 15–20 cm small fault-scarp produced in the hillslope deposit (HSD). (c) General view of small scarp displacing the talus slope of the Mejillones Fault-scarp.

and D, respectively, and the thickness variation is 1.1 ± 0.4 m. This suggests a minimum coseismic displacement of 2.2 ± 0.8 m during the event that produced CW1. In the case of CW2, we measured thicknesses of 1.1 m, 1.5 m, 0.71 m, and 0.72 m in trenches B, C, D and E, respectively, thus the thickness variation is 1.1 ± 0.4 m. This is identical to that detected in CW1 and we infer that an event caused a minimum of 2.2 ± 0.8 m coseismic displacement to produce the CW2 deposit. Although HSD1 is not related to a single seismic event, we measured its thickness to estimate the cumulative displacement during the deposition of this unit. We obtained values of 0.7, 1.3, 0.5 and 0.4 m in trenches A, B, C and D, respectively, with a mean of 0.7 m. This suggests a minimum cumulative displacement of 1.4 m. The colluvial wedge CW3 exhibits a thickness of 0.35 ± 0.05 m that indicates a vertical slip of 0.7 ± 0.1 m. By adding the displacements derived above we obtain 5.4 m of cumulative displacement since the beginning of Surface S2 uplift.

7. OSL Ages of Colluvial Deposits at the Fault Scarp

[25] In order to constrain the ages of the colluvial deposits exposed in trench walls, we collected seven samples for

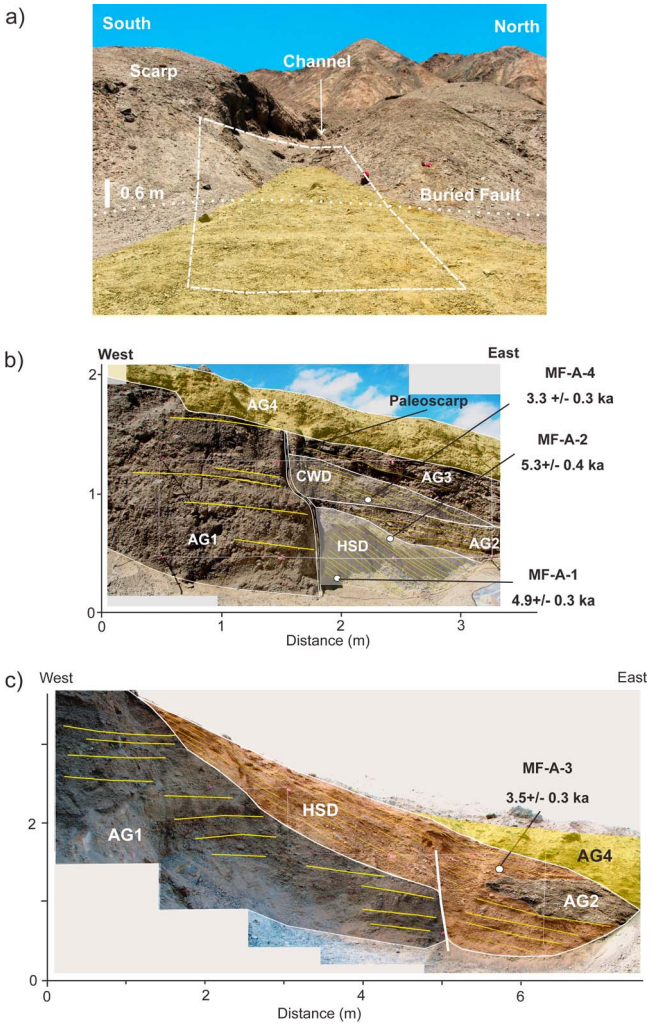


Figure 9. (a) Shows the trench A site. (b) Log of trench A, northern wall. (c) Log of trench A southern wall. White circles in trench logs depict location of samples for OSL dating method. AG1 to AG4: alluvial gravels from older to younger. CWD: colluvial wedge deposit. HSD: hillslope deposit.

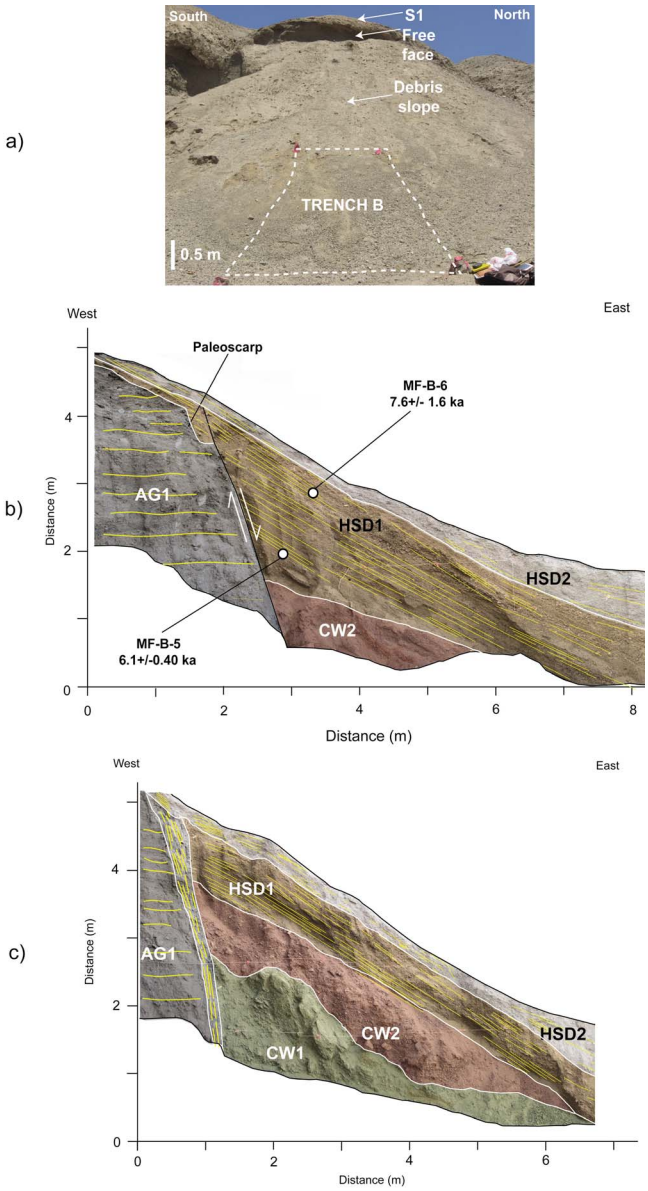


Figure 10. (a) Shows the trench B site. (b) Log of trench B northern wall. (c) Log of trench B southern wall. AG1: alluvial gravels. CW1, CW2 and CW3: colluvial wedges, from older to younger. HSD1: hillslope deposit affected by the fault. HSD2: hillslope deposits not displaced by the fault.

Optically Stimulated Luminescence (OSL) dating. The objective of this dating methodology is to determine the burial age of the sediments that were deposited shortly after a paleoearthquake. The sand sizes usually used in OSL dating range between 90 and 250 μm, though the 125–180 μm or 180–212 μm fractions are thought to be better bleached than the smaller sand-size fractions [*Wintle and Murray*, 2006]. The units targeted for sampling were the hillslope deposits (HSD) with lithic arenite or sub-feldspathic composition, moderate sorting, granular-coarse-medium sand grain sizes, and horizons that are cm – dcm thick, although some colluvial wedge deposits (CWD in trench A) were also sampled. The samples were collected using light-tight plastic tube sizes (2 cm to 3 cm diameter and 10–15 cm long) to minimize mixing across discrete horizons, and some horizons were sampled twice to increase the volume of material. The duplicate samples were processed and analyzed separately. Sample locations are shown in trench logs. Four samples were collected in trench A; two from the hillslope deposit (HSD) and one from the colluvial wedge (CWD) exposed in the northern wall, and one sample from the hillslope deposit (HSD) exposed in the southern wall. In trench B, we collected two samples from the hillslope (HSD), while in trench C one sample was extracted from the same unit, at ~50 cm below the surface.

[26] The fault-related sediments have broad distributions and have multiple components, and this is most likely due to partial bleaching. The transport distances for these fault-generated colluvial samples may be very short, leaving

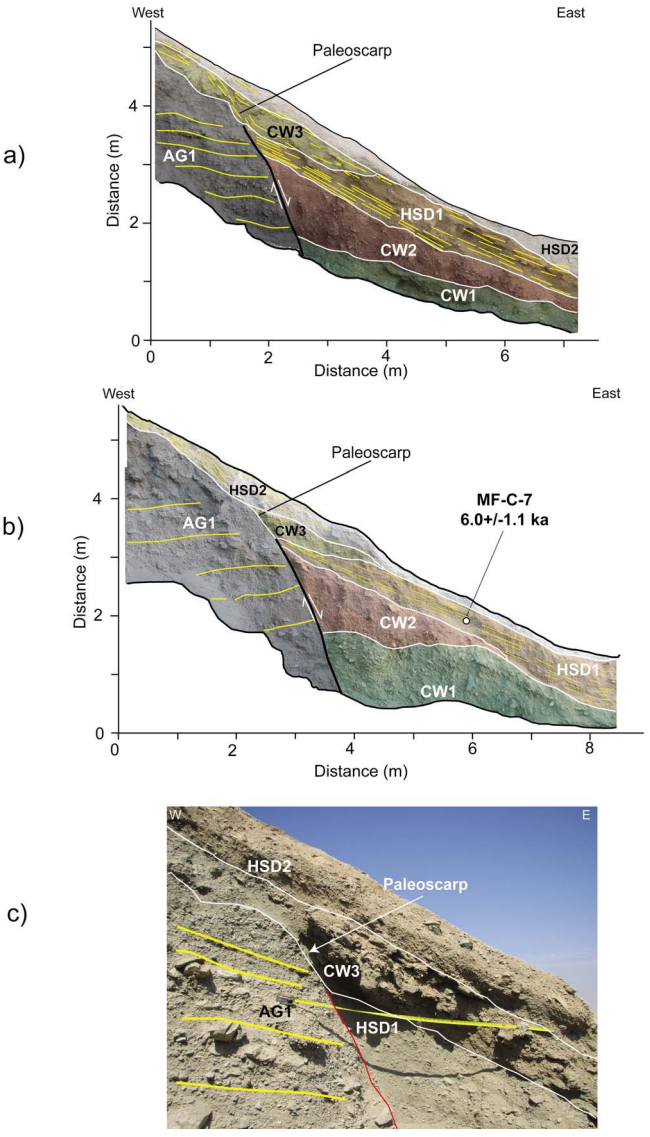


Figure 11. (a) Log of trench C, northern wall. (b) Log of trench C southern wall. Samples sites for OSL dating method are depicted by white circles in trench logs. (c) Picture showing the paleoscarp and CW3 unit. AG1: alluvial gravels. CWD1, CW2 and CW3: colluvial wedge deposits. HSD1 and HSD2: hillslope deposits.

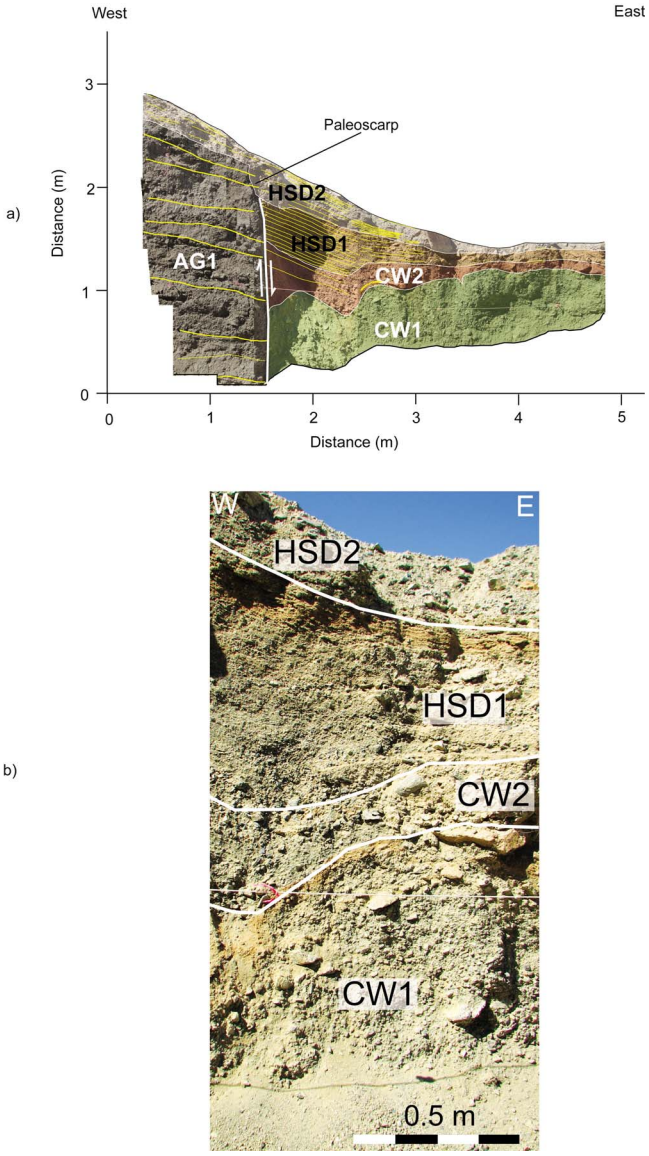


Figure 12. (a) Log of trench D northern wall. (b) Picture showing the red horizon between CW1 and CW2. Also, the contact between HSD1 and HSD2 is depicted. AG1: alluvial gravels. CWD1 and CW2: colluvial wedge deposits. HSD1 and HSD2: hillslope deposits.

insufficient time for mineral bleaching; however, the low erosion rates expected in these settings means that some minerals are exposed to light for very long periods of time and that these minerals should be bleached prior to deposition. Finite age modeling (FAM) shows 2 ages distributions that are consistent with the stratigraphic relationships observed in the trenches.

[27] Table 1 and Figure 15 show the OSL ages obtained in this investigation. Samples from trench A produce a consistent set of ages within the uncertainty of the measurements; the lower samples from the hillslope deposit (HSD) were deposited about 5 ka ago (MF-A-1 and -2). These two samples show the same age within error; therefore we are not able to discriminate different ages for these samples. The sample from the wedge shaped deposit CWD (MF-A-4), which covers the hillslope deposit HSD in the northern wall, produces a stratigraphically consistent younger age of 3.3 ± 0.3 ka. The sample MF-A-3, coming from the upper portion of deformed (HSD) in the southern wall, is also consistent with the age of the colluvial wedge deposit (CWD). It indicates that this part of the hillslope deposit accumulated at 3.3 ± 0.3 ka ago, contemporaneous with the deposition of (CWD). Deformation of the hillslope ceased at least 3.4 ka ago.

[28] Two hillslope deposit samples were collected from Trench B; one from the base of the deposit (HSD1) and another toward the top in the northern wall of the trench. Sample MF-B-5, extracted at the base, gave an age of 6.1 ± 0.4 ka, while the sample MF-B-6, collected from 50 cm below the topographic surface, gave an age of 7.6 ± 1.6 ka. Considering the large uncertainty of the top sample, both samples overlap in age and are consistent with age of the hillslope deposit in trench A. The lower sample indicates that this material started to accumulate ~6.1 ka ago and this represents a minimum age for the underlying colluvial wedges (CW1) and (CW2).

[29] In trench C, the sample MF-C-7, collected from the hillslope deposit, gave an age of 6.0 ± 1.1 ka. This value is consistent with the ages obtained in the hillslope deposits in

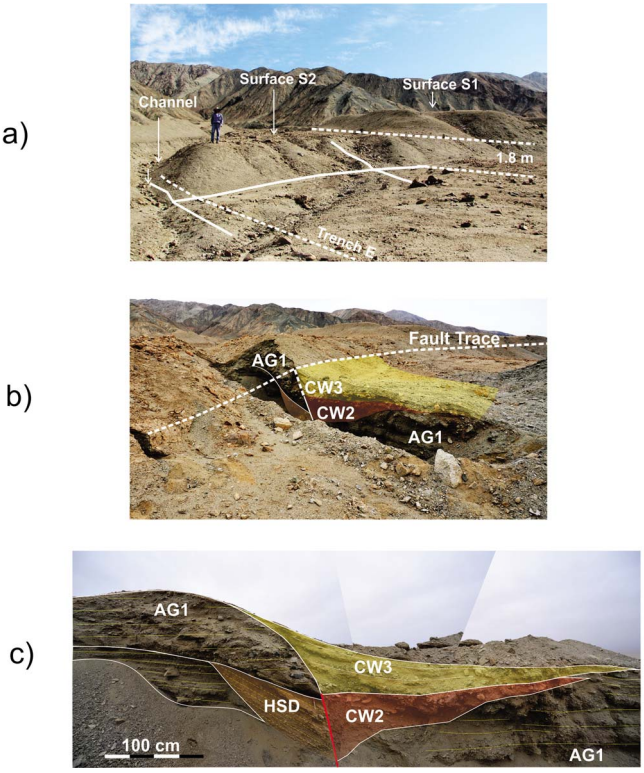


Figure 13. (a) Spatial relation between Surface S1 and Surface S2 at trench D-E sites. The channel to the left is deeply incised, dissecting Surfaces S1 and S2. Location of trenches D and E is also depicted. (b) View of trench E site. White dotted line corresponds to the fault trace. The units identified at the northern wall (CW1, CW2, CW3 and HSD) were detailed logged and are presented in Figure 13c. (c) Trench E log. AG1: alluvial gravels. CWD1, CW2 and CW3: colluvial wedge deposits. HSD1: hillslope deposit.

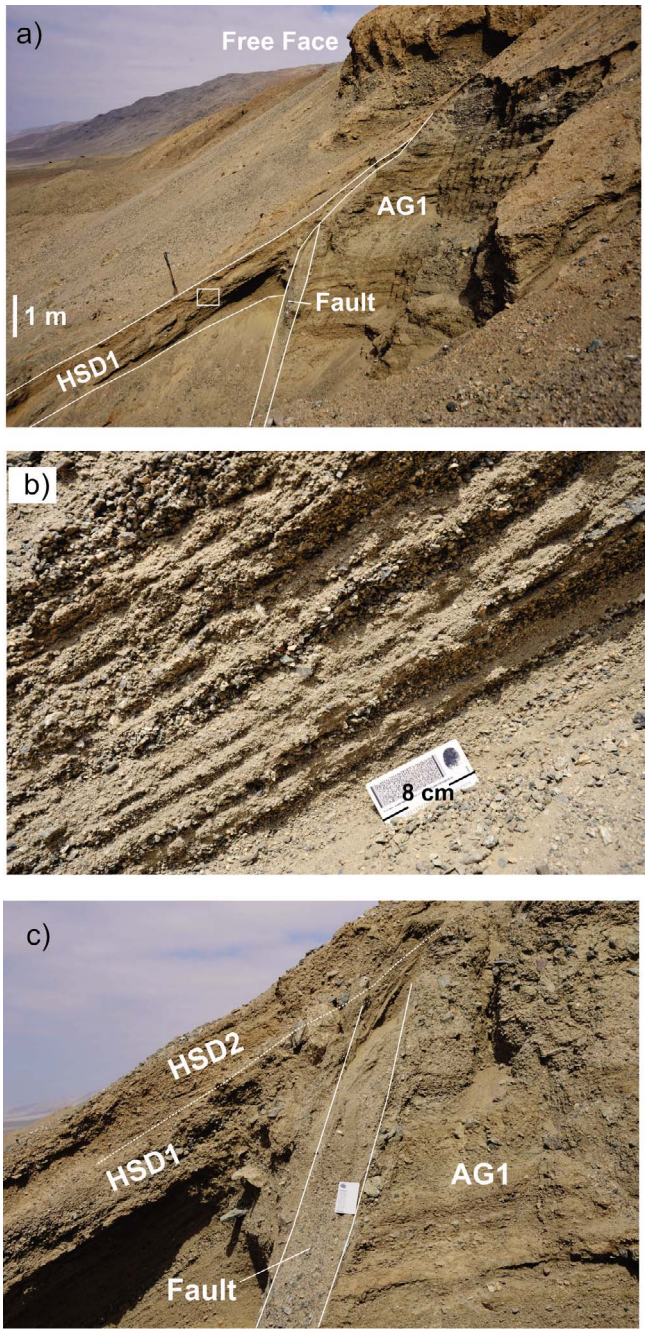


Figure 14. (a) View of trench B site. AG1 in the footwall is clearly stratified. At this site the fault cuts the HSD1 unit. The white rectangle in the HSD1 unit corresponds to the detailed picture showed in Figure 14b. (b) Detailed view of the HSD1 unit. (c) Shows the relation between units AG1, HSD1, HSD2 and the fault. Note that HSD2 seals the fault and is not deformed.

trenches A and B. Because the colluvial wedge (CW3) overlies the dated hillslope deposit this age is a maximum. Since (CW3) has a similar stratigraphic position as the dated colluvial wedge (CWD) in trench A, we suggest that both units represent the last slip event on the Mejillones Fault, with an associated vertical offset of around 1m. Thus, the age of 3.3 ± 0.3 ka obtained in the (CWD), the wedge shaped deposit in trench A, represents the minimum age for the youngest metric-related slip event registered on the Mejillones Fault.

8. Cosmogenic ^{10}Be Exposure Ages

8.1. Previous Data

[30] *Marquardt* [2005] collected samples from the alluvial surfaces dissected by the Mejillones Fault, here named S1 and S2. The exact sample locations are not provided, but yellow rectangles in maps of Figures 3a and 3c correspond to the sampling areas. For Surface S1, *Marquardt* [2005] obtained twelve cosmogenic ^{10}Be exposures ages from large granodioritic blocks partially buried, or buried within the top few meters below the surface of the fan, at a site located 0.5 km northward of our sample site. The Marquardt's study excludes the five oldest of twelve measurements, suggesting these samples have undergone significant pre-exposure, and then derives a mean weighted minimum age of 46.5 ± 3.7 ka, although the weighting applied is not stated (Figure 16). As we will discuss in the following section, we find inheritance corrected ages that suggest the real age is notably younger than this. For Surface S2, *Marquardt* [2005] collected samples from four blocks buried in the fan, at a location within a few meters eastward of our sampling sites. This author suggested that these blocks do not have a significant pre-exposure history, reporting ages that vary between 33.7 ± 6.1 ka and 19.3 ± 4.4 ka, with a mean age of 26.3 ± 1.7 ka. These results are similar to those derived here, but do not reproduce the youngest ages that we find. *Marquardt* [2005] sampled only large blocks (~2 m in diameter), which are more likely to have increased transport times relative to smaller clasts and, hence, a greater inherited cosmogenic ^{10}Be component. In this study we sampled a range of smaller-sized clasts (~10–100 cm), less likely to depend on heavy rainfall to be transported.

8.2. Sample Collection

[31] In order to constrain the ages of the Surfaces S1 and S2, *in-situ* produced cosmogenic ^{10}Be measurements have been made in quartz clasts and granodioritic boulders on, or protruding from, the surfaces. The sites are located in a transfer zone between two segments of the Mejillones Fault (Figures 3c, 3d, and 3f). Here, Surfaces S1 and S2 form part of a relay ramp between the two fault segments. These surfaces are clearly preserved on both sides of the Mejillones Fault and incised by a deep valley. Surface S1 is predominantly planar, with only shallow relief created by localized fluvial incision <1.5 m near the scarp crest. Proximal to the sample sites, from three profiles measured parallel to the scarp, we measured Surface S1 to be 2.8 m higher than Surface S2. Similarly to S1, S2 shows a planar form, although fluvial activity has dissected it more (Figure 17a). Surface S2 is mantled by more granodioritic clasts than S1, ranging in size from pebbles to boulders. Geomorphological features (gravel bar) are better preserved on S2 than on S1 (Figure 17a). The large channel cutting through both S1 and S2 (Figures 3f and 13a) drains eastward, incising between 2 to 6 m through the alluvial fan. The channel bed is made up of coarse grained gravels with abundant granodioritic boulders. Flow in this channel is probably connected with

Table 1. OSL Dating Results of Mejillones Fault Trenches

Sample	U (ppm)	U Uncert (ppm)	Th (ppm)	Th Uncert (ppm)	K (%)	K Uncert (%)	H20[a]	Dose Rate[b] (Gy/ka)	Dose Rate Uncert (Gy/ka)	N[c]	FAM De[d] (Gy)	FAM De Uncert (Gy)	FAM Age[e] (ka)	FAM Age Uncert (ka)
MF-A-1	1.92	0.109	7.587	0.255	2.1	0.029	<2	3.152	0.138	62	15.400	0.57	4.89	0.28
MF-A-2	1.99	0.111	7.76	0.258	1.73	0.027	<2	2.830	0.123	28	15.041	0.99	5.31	0.42
MF-A-3	2.09	0.114	8.11	0.265	1.91	0.028	<2	3.075	0.133	58	10.604	0.72	3.45	0.28
MF-A-4	1.91	0.109	7.682	0.257	1.87	0.028	<2	2.961	0.128	48	9.854	0.59	3.33	0.25
MF-B-5	1.50	0.097	5.993	0.023	1.68	0.026	<2	2.557	0.111	83	15.482	0.76	6.06	0.40
MF-B-6	1.44	0.097	6.301	0.232	1.63	0.025	<2	2.538	0.110	38	19.218	3.93	7.57	1.58
MF-C-7	1.06	0.100	4.387	0.235	1.27	0.026	<2	1.980	0.088	42	11.898	2.06	6.01	1.07

[a]Moisture content (%) based on laboratory measurement loss of moisture on "as received" samples except for RINCON-080109-1 and 2. Negligible moisture content in Mejillones trench samples.

[b]Dose rate is based on in situ measurements of U, Th, and K and includes an ionizing cosmic radiation component following *Prescott and Hutton* [1994] assuming constant burial depth using present-day overburden measurements, altitude, and latitude.

[c]Number of aliquots accepted from SAR analyses.

[d]Finite age modeling (FAM) of equivalent doses (D_e) allows the statistical discrimination of multiple components or a single component in the populations measured, statistical analyses of individual components, and the proportion of aliquots each represents [e.g., *Galbraith et al.*, 1999; *Rodnight et al.*, 2006].

[e]The burial age represents a FAM age.

El Niño events [*Vargas et al.*, 2006], or with unusual winter rains [*Quezada*, 2006]. The lack of any knickpoints along the active channel at the fault trace suggests enough discharge occurs with sufficient frequency for the channel to maintain its grade and transport material eroded from upstream.

[32] To estimate the ages of the S1 and S2 surfaces we collected 6 samples from each for cosmogenic ^{10}Be measurements. This is the number of samples generally assumed sufficient to characterize the ages of deposited features using cosmogenic nuclides [*Putkonen and Swanson*, 2003]. We sampled fragments of quartz-rich schists and granodioritic rocks (Figure 17b). To minimize the possibility that post-depositional erosion or fan surface lowering would influence our results all samples were taken from the flat, planar portions of the fan away from sloping gully sides; and where possible, we sampled rocks protruding several tens of centimeters above the surface (Figure 17b). In locations where such prominent samples were absent, smaller clasts of around 25 cm maximum diameter were collected (see Table 1). In addition, all the selected samples have an iron oxide coating that suggests minimal weathering.

8.3. Assumptions and Age Interpretation

[33] A general assumption required to use cosmogenic nuclides to date sedimentary surfaces is that the concentration of nuclides that accumulates prior to sample deposition (inheritance) is significantly less than that generated during surface exposure [*Repka et al.*, 1997; *Brown et al.*, 1998]. However, the amount of inheritance, or pre-exposure, may be significant in hyperarid conditions, where low rates of erosion and sediment transport are typical. To estimate the potential affect of inherited ^{10}Be produced during pre-exposure and/or transport we applied two strategies. First, we collected alluvium from the active channel that incises the S1 and S2 surfaces (sample MF-D-4, Figure 13a). Assuming the pre-exposure experienced by this channel material is similar to the inheritance that would have been experienced when the fan aggraded we can use it to consider the inherited ^{10}Be component of our surface samples [*Brown et al.*, 1998]. Second, from a pit dug in the wall of the valley incising S1 and S2 (Figures 3f and 13a) we collected three rock samples (1.25, 2.85 and 3.60 m depths) and one sample consisting of sand, pebbles and alluvial gravels (4.60 m depth) (Table 2). The main production mechanism for cosmogenic ^{10}Be in quartz is spallation of O by high-energy neutrons. In sedimentary materials with a density of 1.8 g/cm^3, the ^{10}Be production at 3.60 m will have been reduced to <2% of the surface rate [*Lal*, 1991], such that the samples from this depth and below are essentially shielded from the point of burial onwards. There will be minor production due to the muogenic component of the cosmic rays and potentially radiogenic production; in addition there will be a small amount of loss due to the radioactive decay of the ~1.36 Ma half-life of ^{10}Be, but we assume these affects to be negligible here. This strategy has been shown to be able to correct for fan sample pre-exposure assuming that subsurface material was rapidly buried around the same time as the overlying surface was deposited [*Anderson et al.*, 1996]. The ages that we obtained for all samples are given in Table 2.

[34] Scatter in fan surface sample ages is usually the product of variable transport histories, and thus pertains to pre-exposure, or it is due to differential erosion and/or disturbance of the clasts after deposition [*Brown et al.*, 1998; *Behr et al.*, 2010]. Erosion of the clasts on the fan, or lowering of the fan surface such that previously buried clasts

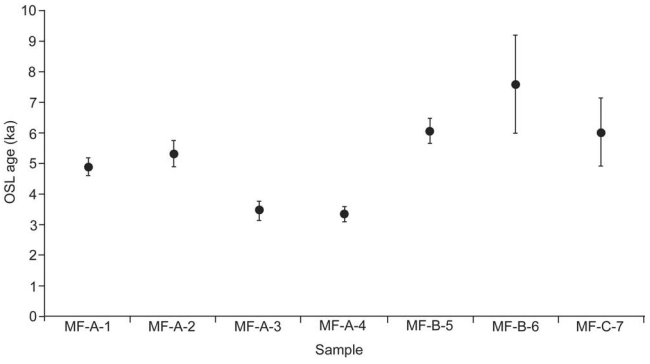


Figure 15. Plot showing the OSL ages (1σ uncertainties) obtained from trenches dug along the Mejillones Fault.

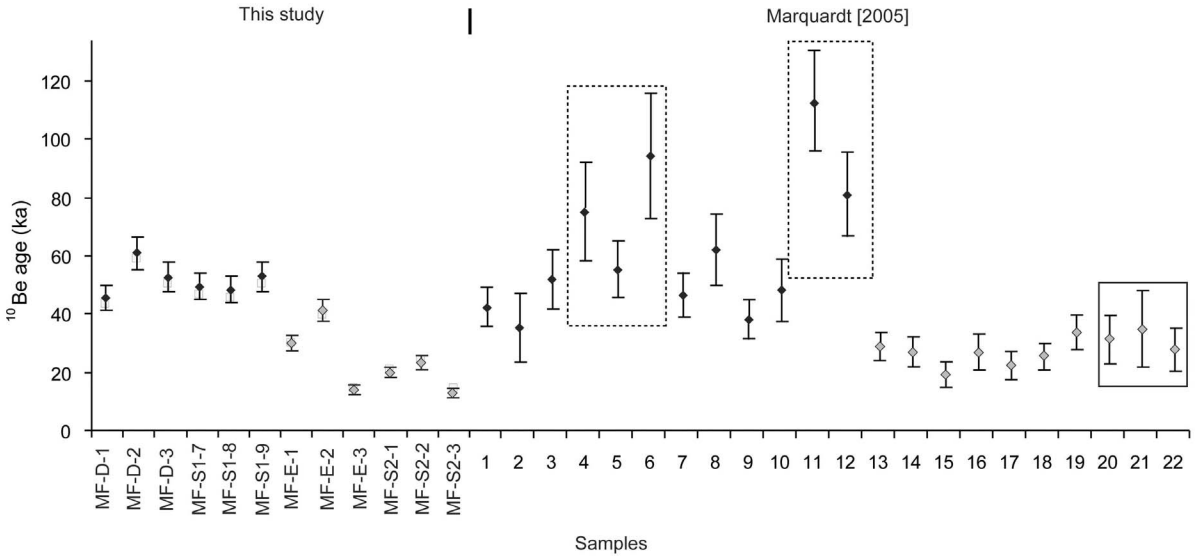


Figure 16. Plot showing the ^{10}Be ages (1σ uncertainties) obtained by *Marquardt* [2005] and in this work for the alluvial surfaces in the study area. Black diamonds are samples from Surface S1 and gray diamonds are samples from Surface S2, according to *Lal* [1991] scaling factor. For our samples, the ages were calculated according to the scaling factors of *Dunai* [2000]. We also calculated our ages according to scaling factors of *Lal* [1991] to allow direct comparison with Marquardt and these are depicted by light gray squares. Dashed-line boxes highlight those samples that *Marquardt* [2005] considered had ^{10}Be inheritance, and that were not considered in his calculations. The segmented line boxes highlights the pit samples of *Marquardt* [2005].

become exposed, will artificially reduce fan surface ages. Estimates of boulder and bedrock erosion rates in the hyperarid regions of northern Chile are typically less than, or on the order of, 1 m/Ma [*Kober et al.*, 2007; *Placzek et al.*, 2010]. We estimate the age bias that would be introduced if our S1 surface samples had been undergoing erosion of 1 m/Ma for 45 ka and find it would reduce the ages by <10%, hence some of the scatter between these samples may be explained by variable erosion. To minimize the influence that fan surface lowering would have on our results we followed the sampling criteria presented in section 8.1. Although the potential for fan surface lowering and clast erosion is difficult to discount, our findings from the shielded samples that are discussed below suggests the scatter in our data is best explained as being caused by changes in the predepositional exposure.

[35] Using the two different sampling approaches above (active channel sampling and shielded samples) we

Table 2. The ^{10}Be Ages Obtained in the Study Area

Sample ID	SUERC AMS ID	Surface/ Burial Depth	Latitude	Longitude	Altitude (m)	Sample Thickness (cm)	Shielding Factor	^{10}Be Concentration ($\times 10^3$ at/g)	σ^{10}Be Concentration ($\times 10^3$ at/g)	Age[a] (years)	σ Age (years)
MF-D-1[b]	b3727	S1	−23.13446	−70.50214	168	2	0.99	171	5	43,400	5,300
MF-D-2[b]	b3728	S1	−23.13463	−70.50178	165	3	0.99	225	6	59,100	7,200
MF-D-3	b3729	S1	−23.13473	−70.50204	171	5	0.99	193	5	50,100	6,100
MF-S1-7	b4347	S1	−23.13453	−70.50226	179	6	1.00	188	6	48,300	5,900
MF-S1-8	b4348	S1	−23.13468	−70.50199	179	5	0.99	184	6	47,200	5,800
MF-S1-9	b4349	S1	−23.13463	−70.50196	170	5	0.99	199	6	52,100	6,400
MF-S2-1	b4350	S2	−23.13535	−70.50175	163	6	0.99	72.7	2.6	20,900	2,600
MF-S2-2	b4352	S2	−23.13535	−70.50175	156	6	0.99	84.2	2.9	24,100	3,000
MF-S2-3	b4353	S2	−23.13535	−70.50175	159	5	0.99	47.0	1.9	13,700	1,700
MF-E-1	b3731	S2	−23.13545	−70.50171	164	5	1.00	111	3	30,300	3,700
MF-E-2	b3733	S2	−23.13545	−70.50171	164	4	1.00	152	5	39,600	4,900
MF-E-3	b3734	S2	−23.13545	−70.50171	164	4	1.00	51.3	3	14,600	1,900
MF-D-4[c]	b3730	Channel	−23.13592	−70.50149	na	na	na	280	7	na	na
MF-ESC-2[c]	b4956	125 cm depth	−23.13454	−70.50230	na	na	na	99.1	3.4	na	na
MF-ESC-1[c]	b4955	285 cm depth	−23.13454	−70.50230	na	na	na	42.9	2.2	na	na
MF-ESC-3[c]	b4957	380 cm depth	−23.13454	−70.50230	na	na	na	56.7	2.5	na	na
MF-S1-5[c]	b4346	460 cm depth	−23.13454	−70.50230	na	na	na	87.6	3	na	na

[a]These ages are not corrected for inheritance; see text. Input into CRONUS-Earth online calculator (v. 2.2) also includes density of 2.6 g/cm^2 and the standard atmospheric pressure flag. Erosion is assumed to be zero (see main text and auxiliary material for discussion of the cosmogenic ^{10}Be calculations).
[b]Samples collected from partially buried rocks protruding above the fan surface.
[c]Samples collected to determine potential ^{10}Be inheritance. See text for discussion.

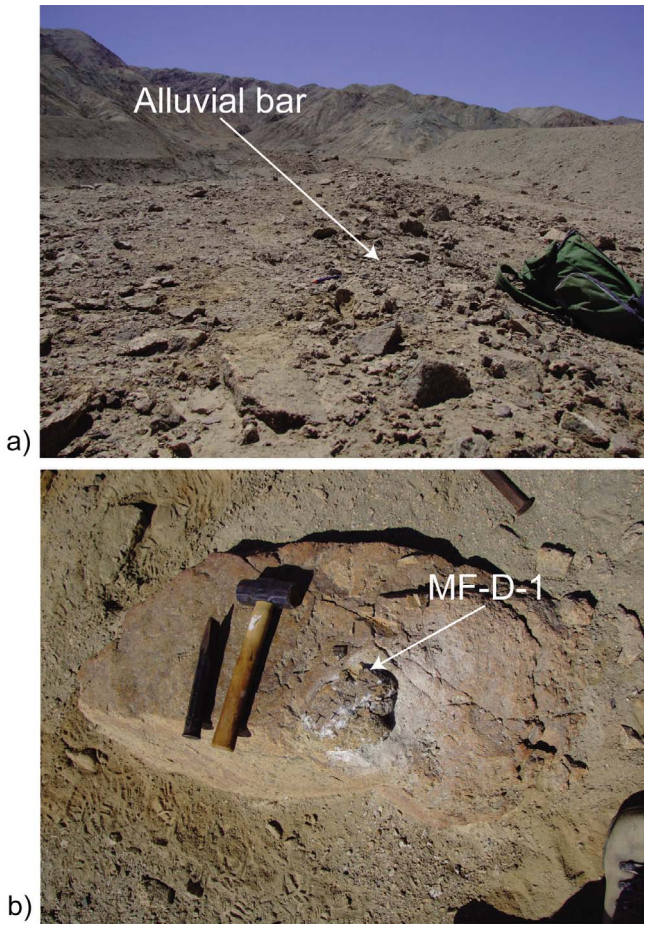


Figure 17. (a) Shows the aspect of Surface S2. White arrow indicates an alluvial bar where some samples were collected. (b) Picture showing a meter-scale boulder buried in Surface S1. From this rock we collected the sample MF-D-1.

considered the influence of possible pre-exposure on the samples. The ^{10}Be concentration in the active channel sample is greater than the concentration in the samples on the S1 surface, indicating that we cannot use the concentration of ^{10}Be in the channel sample (MF-D-4) to determine the inheritance. The greater concentration of ^{10}Be in the channel material as compared to the surface can be explained as a reduction in the erosion rate at the source area of the fan material after S1 aggraded. Alternatively, the sample collected in the channel may include reworked material with a complex burial and transport history that has involved periods of surface exposure upstream.

[36] The four samples collected from different depths below S1, on the other hand, have a range of ^{10}Be concentrations that are all less than samples at the surface. Assuming the ^{10}Be in the shielded, sub-surface samples was inherited before the samples were buried, and normalizing the concentrations to the depth of the deepest sample to minimize any minor post-depositional production (4.60 m, Figure 18), suggests the range of pre-exposure concentrations of the pit samples varies by 56×10^3 atoms/g (illustrated by Y on Figure 18). The variability of ^{10}Be concentrations measured in the surface samples is similar to this value, approximating 53×10^3 atoms/g. Thus, the degree of variation in ^{10}Be concentrations from samples on the surface of S1 can be explained by the variable exposure of the samples prior to their deposition. Clast erosion or fan surface lowering may play a minor role in producing the scatter in the ^{10}Be concentrations on S1, and this could explain why some surface samples have concentrations lower than the concentration-depth curves predict (Figure 18). However, differing amounts of inheritance is most probably the first order cause for the variation in concentrations observed in the surface samples. While the scatter in the surface and subsurface samples is similar, the magnitude of the scatter could increase if more samples were collected, in particular from the subsurface where the concentration variability is derived from only four samples. If inheritance is causing the scatter, the youngest age will be the most robust, because it represents the age least influenced by the pre-depositional history. The youngest age derived from the ^{10}Be of the S1 samples is 43.5 ± 5.3 ka (Table 2). However, as we can base an estimate for the inheritance on the concentrations of the sub-surface samples, we can derive values for the inheritance corrected surface concentration. Plotting a cosmogenic nuclide profile curve through the sample concentrations at various depths, and assuming the pre-exposure is equal in all samples, is an approach sometimes used to quantify inheritance [*Granger and Smith*, 2000]. In this case, the variable amounts of pre-exposure, typical for large clasts [*Matmon et al.*, 2005],

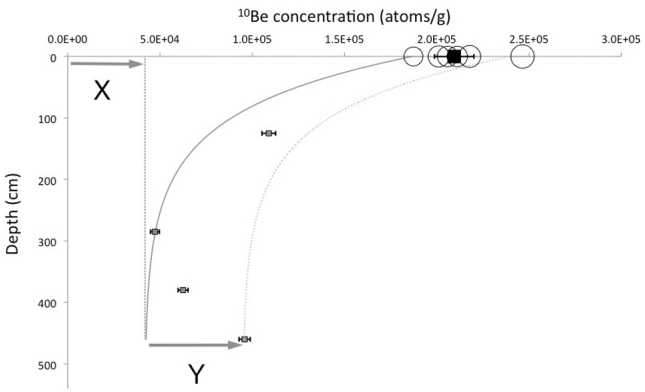


Figure 18. Plot showing the ^{10}Be concentrations of the S1 surface (circles), and the depth versus ^{10}Be concentrations of the S1 subsurface (gray squares). The solid black square on the surface is the error weighted mean of the surface sample results and associated variance. The 1σ uncertainties of the surface sample concentrations are given by the diameter of the circles. The 1σ uncertainties of the subsurface samples are indicated. All uncertainties incorporate analytical measurement errors only. The solid gray curve indicates the production profile extended through the sample with the lowest inherited component. When compared with the dotted gray curve, showing the concentrations extended thorough the sample with the highest inherited component, it can be seem that scatter in ^{10}Be concentrations at the surface are similar to those at depth, as illustrated by arrow Y. The vertical gray dotted line and arrow X reflect the amount of inheritance assumed when deriving an age for the surface (see text).

prevent a straightforward fit to the samples at depth. However, the similar amounts of scatter in our surface and subsurface data sets suggest a curve plotted through the shielded sample with the least pre-exposure will be adequate to approximate the inheritance in the surface sample with the least ^{10}Be concentration. That is, we use the subsurface sample with the least inheritance to correct the surface sample with the least inheritance. The concentration-depth profile curve shown on Figure 18 suggests the ^{10}Be inheritance, extended to depths from the lowest concentration sample, is $\sim 3.73 \times 10^4$ atoms/g (illustrated by X on Figure 18). This equates to $\sim$22% of the total concentration of the corresponding lowest concentration surface sample. Correcting for this pre-exposure and deriving an age from this value gives 35.4 ± 3.3 ka (using the Cronus online calculator [*Balco et al.*, 2008]). This "inheritance corrected age" is the most probable age for the deposition of Surface S1. We note that *Marquardt* [2005] uses the production rate latitude and altitude-scaling scheme of *Lal* [1991], whereas we prefer to use the scaling scheme of *Dunai* [2000]. If we recalculate our inheritance corrected age with the *Lal* [1991] scaling scheme used by *Marquardt* [2005] we get an age of 35.5 ± 3.4 ka (using the Cronus online calculator). We conclude that the mean inheritance corrected age of 46.5 ± 3.7 ka reported by *Marquardt* [2005] is somewhat older than our estimate, probably due to the different ways in which inheritance has been dealt with in the two studies.

[37] From S2 we obtained six ages that are consistently younger than the S1 samples, but which show a larger degree of scatter, varying between 39.6 ka to 13.7 ka. This scatter indicates that these clasts have had variable pre-exposure histories, or undergone post-depositional disturbance. Possible scenarios to explain the data from S2 are that the processes involved in the surface construction promoted the deposition of reworked clasts. Surface S2 appears to be a fluvial terrace, where lateral stream incision has eroded $\sim$2.8 m depth of fan material before uplift on the Mejillones fault and abandonment of the surface. Surface S2 is relatively narrow and lies parallel to the currently active channel, and on it we identified clast deposits indicative of alluvial channel bars (Figure 17a). Therefore, creation of this surface by erosion of older fan deposits could explain the greater degree of scatter in the ages we measured, as compared to S1. That is, the incision into older material could result in intermingling of 'fresh' alluvium with prior deposits. This scenario explains the existence of ages as old as $\sim$39.6 ka (sample MF-E-2) as having undergone significant pre-exposure before deposition at the sample site. Thus, the youngest age we record is probably the most reliable age for the abandonment of this surface, i.e., close to 13.7 ± 1.7 ka, while the scatter in the S2 data represents the variable amount of inheritance present in these samples. Figure 16 depicts a comparison between the ages obtained by *Marquardt* [2005] and our results for both Surfaces S1 and S2. Again we note that this author used a different scaling scheme [*Lal*, 1991] from us [*Dunai*, 2000] and hence we have decided to present our data according both scaling schemes, though the difference in ages obtained using the different scaling schemes are small. The ages that *Marquardt* [2005] obtained for Surface S2 show less scatter than we find. This author considers that the inherited ^{10}Be component is negligible for the ages from this surface, hence validating his mean uncorrected estimate (ca. 26 ka). Nevertheless, due to the complex history involved in the construction of Surface S2, the youngest age we obtain (ca. 13.7 ka) is most likely to be the least affected by pre-exposure, and is therefore more representative of the timing of abandonment of Surface S2. Based on morphostratigraphic relationships and ^{14}C dating of debris flow events *Vargas et al.* [2006] proposed that the present-day aridity has prevailed since 5.7 ka, but that every $\sim$40 years aridity gives way to heavy rains associated with ENSO events. Because the maximum run-off from these events is localized we suggest the recurrence interval in any specific valley could be longer. *Vargas et al.* [2006] did not find evidence for heavy rains between 15 to 5.7 ka, but mapped older alluvial fans that were active between 15 ka and 30 ka, suggesting that heavy rains occurred during this time span. The age we estimate for the formation of Surface S2 by lateral channel migration agrees, within uncertainties, with this period of intensified fluvial activity, whereas the inheritance corrected age of the Surface S1 somewhat predates it.

[38] Last, we note the quoted uncertainties in the cosmogenic ^{10}Be ages presented here incorporate only analytical and production rate uncertainties, and do not take into account the potentially large uncertainties associated with assigning values for inheritance. When deriving slip rates based on the age of Surface S1 we cater in part for uncertainties associated with pre-exposure by deriving an applicable range of slip values based on both inheritance corrected and uncorrected ages. In the case of the slip rate derived from Surface S2, the influence of inheritance and/or post-depositional disturbance or erosion is hard to quantify. Hence, care is taken when interpreting the age and subsequent slip rate of S2 in particular, as unlike Surface S1, the estimate of inheritance is based on the scatter in the surface ^{10}Be concentrations only.

9. Discussion

9.1. Local Morphology, Trench Sedimentary Record and Fault Activity

[39] In order to reconstruct the paleoseismological history of the Mejillones Fault we summarize the fundamental observations made from the local morphology and trenches. These key observations constitute the basis of our understanding of the Mejillones Fault activity over the last 35 ka.

[40] 1. The local morphology along the trace of the Mejillones Fault is dominated by a compound fault scarp that cuts the eastern piedmont of the Mejillones Horst. The first order morphological feature is the fault scarp itself which was formed after $\sim$35 ka. The fault scarp changes its morphological expression along its 40 km long trace. At the northernmost end the fault scarp is continuously expressed along an 8 km surface rupture evident in alluvial sediments of the eastern piedmont. This rupture is composed of two segments that join in a relay ramp near the middle. Along this 8 km long rupture, surface offset changes from several centimeters in the south, to $\sim$10 m in the north, with $\sim$15 m vertical offset in the middle section. The scarp aspect of the segments north and south of the relay ramp is identical, suggesting that they have the same age. Southward, the scarp is discontinuous in Quaternary alluvial and marine sediments.

[41] 2. Along the northern extension of the fault trace, scarp evolution was contemporaneous with the development of four alluvial surfaces. The two oldest surfaces (S1 and S2) occur in places where the fault intersects three large valleys. These surfaces were abandoned by fault slip at ~35 ka (S1) and ~14 ka (S2) ago. The oldest surface is preserved mostly on the highest part of the piedmont, the younger surfaces (S3 and S4) show centimeter-scale vertical offsets, and S4 represents the present-day surface of active cones localized at the base of the scarp. In the places where the fault underlies the active cones, we find that they are affected by fault deformation. Generally, the upper parts of the cones beds (40–70 cm below the surface) show no evidence of fault deformation. OSL data show that the undeformed alluvial-colluvial material is younger than 3.3 ± 0.3 ka (average OSL age of the undeformed hillslope deposit and age of CWD).

[42] 3. Midway up the scarp, the topographic profile shows a sharp break in slope angle. The altitude of this break in slope coincides with the minimum elevation Surface S2, and upper part of the scarp maintains a lower gradient (25–30°) and three additional minor breaks in slope. The lower part of the scarp has a slope of 30–35° and the trenches were excavated in this portion.

[43] 4. Trench logs show deposition histories after the abandonment of Surface S2. Lower sections show two colluvial wedges and hillslope deposits form an upper section. A third colluvial wedge was observed in two trenches excavated in the northern segment. This unit is younger than the underlying hillslope deposit (HSD1). According to cosmogenic ^{10}Be ages and the OSL determinations, the lower colluvial units (CW1 and CW2) were deposited after 13.7 ± 1.7 ka and before 6.1 ± 0.4 ka. The deformed hillslope deposit (HSD1) accumulated in a time span between 6.1 ± 0.4 ka and 3.3 ± 0.3 ka. The younger colluvial wedge (CW3, CWD) was deposited shortly after 3.3 ± 0.3 ka BP. This younger colluvial wedge divides the hillslope deposit into a lower section cut by the fault, and an undeformed upper section. These estimations are in agreement with U-series disequilibrium ages in co-seismic gypsum fractures fills and exposed fault planes of the Mejillones Fault that set the occurrence of large paleoearthquakes at ca. 29.7 ± 1.7 ka, 11 ± 4 ka and 2.4 ± 0.8 ka [*Vargas et al.*, 2011].

9.2. Seismic Paleomagnitude Estimates

[44] According to *Mason* [1992], if we consider the locations of our trenches as having been selected at random, the amount of vertical offset suggested by colluvial wedge thicknesses can be assumed to be close to the average thickness, rather than the maximum. Other studies consider that the displacement measurements in trenches are equal to the maximum displacement, especially if the trench was excavated at the center of a fault segment where in general the surface displacements tend to be largest [*McCalpin*, 1996]. Here, we follow a more conservative approach and assume the estimates of slip magnitude are more accurately expressed by the average displacement. We measured colluvial wedges that have experienced some erosion after deposition; therefore, the documented thicknesses are a minimum for estimates of vertical slip. The thicknesses for the CW1 and CW2 are identical (1.1 ± 0.4 m). Following the estimation of *McCalpin* [1996], who suggests that the thickness of colluvial wedges shed from scarps approximate half the height of the scarp, the paleoearthquakes that produced the colluvial wedges CW1 and CW2 created scarps as high as 2.2 ± 0.8 m. Nevertheless, it must be stated that because the observed colluvial wedges probably experienced some erosion after deposition the magnitude derived is a minimum. These values are representative of the average co-seismic slip during each event. We used the relationships of *Wells and Coppersmith* [1994] to estimate earthquake paleomagnitudes from average co-seismic slip. According to their empirical relationship, we propose that two earthquakes with Mw (moment magnitude) 7.0 ± 0.2 generated the colluvial wedges, CW1 and CW2. *Wells and Coppersmith* [1994] also made regressions between moment magnitude and rupture length of normal fault. If we consider a total length of 40 km for the Mejillones Fault, taking into account its onshore length and the projected submarine continuation, the paleoearthquakes produced by this normal fault should be of Mw 6.8, a value that agrees well with our estimates from average co-seismic slip.

[45] The colluvial wedge CW3 has a thickness of 0.35 ± 0.05 m, indicative of an associated rupture producing 0.7 ± 0.1 m of vertical slip on the Mejillones Fault. This corresponds to a moment magnitude of 6.6 ± 0.1. The smallest and youngest offset that we observed affecting the scarp slope and Surface S3 (the cm-scale scarps) probably represents the minimum magnitude of faulting able to produce near surface geomorphic features. According to *Wells and Coppersmith* [1994], this minimum magnitude is near Mw ~ 5 event. However, it is necessary to consider that other factors can control surface expression of an earthquake, such as the hypocenter depth and the displacement distribution along the rupture plane. For example, events like the Mw 6.9 in 2010 produced by the Pichilemu Fault [*Arriagada et al.*, 2011] did not produce surface ruptures.

9.3. Hillslope Process and Faulting

[46] As previously mentioned, we suggest that the first order controls on the accumulation of hillslope deposits downward of the middle part of the scarp are by successive gravitationally controlled grain flows. The layered fabric of the HSD formed due to sedimentation of normally graded thin beds of granules and sand since ~6.1 ka. This accumulation was interrupted by the occurrence of the last large event on the fault at ~3.3 ka that generated the colluvial wedge CWD and CW3.

[47] Although free face degradation is the process promoting the HSD accumulation, we propose that normal faulting controls the deposition of this unit. We base this proposition in the fact that the hillslope deposit HSD1, exposed in vertical sections of the trenches, shows a conspicuous difference in thickness between the footwall and the hanging wall, with greater thickness in the downthrown block (Figure 10b). This geometry is similar to growth strata related to normal faults. In this sense, we suggest that HSD1 accumulated in the hanging wall by downward slip along the Mejillones Fault. An important question to resolve is whether this HSD1 deposit accumulated progressively with downward displacement of the eastern part of the fault, or if HSD1 accumulated after a single displacement event. In the first case, grain flow events accumulated and were progressively displaced downward by localized shearing in the fault

plane. In the second case, the HSD1 deposit accumulated in a period of fault quiescence and later experienced downward displacement in a single event at around 3.3 ka (the age of CW3 and CWD). During this event the fault would cut all the previously accumulated HSD1. We suggest that the latter scenario is less feasible because it contradicts a fundamental geological fact; the position where the hillslope deposit reaches its maximum thickness is the part of the scarp profile where the eroded material coming from up-slope should have not accumulated. Based on this we suggest that the Mejillones Fault experienced a change in its seismic behavior at ~6.1 ka, and that this involved a change from episodic meter-scale vertical slip to centimeter-scale vertical displacements between ~6.1 and ~3.3 ka. We suggest two scenarios by which this could occur. One is by supposing continuous and non-seismogenic fault slip, and the other is by clustering of small and shallow earthquakes (Mw < 5). We are not able to discriminate between these two scenarios with the available data. Whatever the case, this situation was interrupted by the occurrence of a moderate event, as is suggested by the existence of CW3 and CWD. Therefore, continuous slip or small events on the fault operated until ~3.3 ka. If we accept that at ~6.1 ka there was a change in the seismic behavior of the fault, we have to explore some processes able to control this change. One possible explanation is that after the second Mw ~ 7 earthquake, the fault experienced a significant drop in stress. We suggest that the two Mw ~ 7 earthquakes that produced the colluvial wedge deposits (CW1 and CW2) took place during a time when the fault had a high level of stress. Even after the occurrence of the first Mw 7 earthquake, the stress level remained high enough to generate a second Mw 7 event. Not until after this second event did the fault reach the stress state that characterizes the period during which the hillslope deposit HSD1 was accumulated. Relative to this tentative change in the stress state, it is worth noting that we base this suggestion only on the paleoseismic observations made at the Mejillones Fault. We do not consider more complex scenarios supposing the simultaneous reactivation of other nearby faults, for example the Caleta Herradura Fault.

9.4. Slip Rates and Recurrence Estimation

[48] By combining the topographic data, the trench stratigraphy and the age constraints, we calculated the slip rate of the Mejillones Fault during four time intervals since ~35 ka to the present. The first time interval covers the period from the abandonment of Surface S1 until the formation of the Surface S2. Slip rate during this interval is calculated by dividing the along strike variation of the mean elevation difference between Surface S1 and Surface S2, corresponding to 8.0 ± 6.7 m, by the time between abandonment of S1 and S2. If we assume that abandonment ages of ~35.4 ± 3.3 ka for Surface S1 and 13.7 ± 1.7 ka for S2, the time between these two ages is 21.7 ± 5 ka, resulting a slip rate for this stage of 0.46 ± 0.41 m/ka. We chose to calculate this slip rate using the cosmogenic ^{10}Be inheritance corrected age of ~35.4 ± 3.3 ka, for the reasons discussed in section 8. The second interval corresponds to the time between the abandonment of Surface S2 and the beginning of the accumulation of the faulted hillslope deposit. During this time interval large vertical slip events on the Mejillones Fault formed the colluvial wedges CW1 and CW2. The net displacement deduced from the thickness of these two colluvial wedges in trenches B, C and D and E is 4.4 ± 1.13 m. The time span between Surface S2 abandonment and the beginning of the hillslope accumulation is 7.6 ± 1.7 ka, and consequently the calculated slip rate is 0.64 ± 0.29 m/ka. The third time interval covers the period in which the HSD1 deposit was accumulated and faulted. We calculated the average slip rate by dividing the vertical offset suggested by the mean thickness of the HSD (1.4 ± 0.2 m) by the span time over which it was formed, based on the age of the lower OSL sample (6.1 ± 0.4 ka) and the OSL age of the undeformed hillslope deposit (3.3 ± 0.3 ka). This yields a net slip rate of 0.56 ± 0.17 m/ka. The fourth interval covers the time during the accumulation of CW3 or CWD and the undeformed HSD2. In this interval the contribution to the accumulated vertical slip in the fault is 0.7 ± 0.1 m and the time elapsed since the last earthquake is 3.3 ± 0.3 ka. Dividing the offset by this time period gives a slip rate of 0.22 ± 0.06 m/ka. Considering the number of uncertainties and the assumptions that we have made for the first three intervals we can conclude that the slip rate since ~35 ka to ~3.3 ka was 0.61 ± 0.26 m/ka. Comparing this average slip rate with the slip rate of the last interval it could be interpreted that the fault has experienced a subtle decrease in the slip velocity. However, we think that a lower slip rate of 0.22 + 0.06 m/ka for the last interval is the result of the short time span considered in the calculation. Furthermore, in this estimate we used the contribution made by a lower magnitude paleoearthquake to the vertical slip. Therefore, we prefer to state that the slip rate in the Mejillones Fault has not considerably varied during the last 35 ka.

[49] According to *Slemmons and Depolo* [1986], the recurrence interval of Mw ~ 7 earthquakes on faults with slip rates on the order of 10^{-1} mm/yr is on the order of thousands to tens of thousands of years. *McCalpin* [1996] proposes a procedure to calculate the recurrence interval that consists of dividing the displacement per event by the slip rate. In our case study, we were able to estimate only the slip rate for the second interval using this method. If we consider the displacement per event is equal to 2.2 ± 0.8 m, and the slip rate is 0.64 ± 0.29 m/ka, the recurrence interval for Mw ~ 7 earthquakes is 5 ± 3.5 ka. Nevertheless, it is worth mentioning that this value does not imply perfectly cyclic behavior on the Mejillones Fault. Besides the uncertainties arising from the coseismic displacements that were derived from the thickness of colluvial wedges, this calculation supposes that the earthquake occurrence is a regular process, which is not the case. Therefore, in this situation, we think that the recurrence interval must be understood as a parameter reflecting the level of activity of the fault, and not a value representing exactly the periodicity of a natural phenomenon. With the available data, we can state that the Mejillones Fault is an active fault capable of producing Mw 7 earthquakes, with a probable 'recurrence' interval of 5 ± 3.5 ka, and that it must be considered as such for seismic risk studies in the region.

9.5. Upper Plate Fault Activity and Subduction Earthquake Cycle

[50] Determining the extension of the Mejillones Fault beneath the surface is fundamental to understanding its seismic potential. Rupture areas scale positively with the moment

magnitude of earthquakes, according to *Kanamori* [1977]. Thus, listric faults with detachment levels close to the surface should have lower magnitude earthquakes than subvertical and deeply rooted faults. The linear trace of the Mejillones Fault and field measurements of the dip angle suggests that it is a sub-vertical fault (dip > 70°) for at least several kilometers below the topographic surface. Submarine profiles developed in the Mejillones Bay show that the hanging wall of the fault is not rotated horizontally for amounts larger than 8° near the surface, suggesting that the geometry for the Mejillones Fault is not listric in this case. Although the downdip continuation of the Mejillones Fault to the interplate contact has not been demonstrated, *Husen et al.* [1999] and *Motagh et al.* [2010] identified some seismic aftershock activity in deep structural levels of other upper plate faults close the Mejillones Fault. This suggests that some faults of the upper plate, as with the main branch of the Atacama Fault Zone and the Mejillones Fault, extend sub-vertically and are probably rooted into the seismogenic zone.

[51] Following the regressions for aspect ratio (rupture length per rupture width) versus the rupture length of *Wesnousky* [2008], we estimate the rupture width of the Mejillones Fault. According to this estimation, the paleoearthquakes that we identified slipped to a depth of at least 16 km. This estimation is in agreement with other normal faults, while a deep extension of the seismogenic zone for upper plate faults is in agreement with the low heat flow dominating the coastal region of northern Chile [*Springer and Forster*, 1998].

[52] Because the slip rates on the megathrust represented by the subduction zone are at least two orders of magnitude faster than the slip rates in the Mejillones Fault, and considering that the recurrence of the largest subduction earthquakes in northern Chile are considerably shorter than the largest earthquakes on the Mejillones Fault (120 year for the megathrust [*Comte and Pardo*, 1991] versus our estimate of 5 ± 3.5 ka on the Mejillones Fault for Mw 7 earthquakes), we can state that the upper plate fault activity is not in phase with the largest subduction earthquake cycle. It suggests that stress and strain on upper plate faults build up slowly through several cycles of subduction earthquakes.

10. Conclusions

[53] We have concluded the following.

[54] 1. The Mejillones Fault exposed in the coastal area of northern Chile is an active structure of the upper plate, able to generate Mw ~ 7 earthquakes with a recurrence of 5 ± 3.5 ka.

[55] 2. The average slip rate of the fault between ~35 ka to ~3.3 ka is 0.61 ± 0.26 m/ka.

[56] 3. The fault has produced three large earthquakes during the last 14 ka (two Mw 7 and one Mw 6.6), and we conclude that the cycle of largest earthquakes on the Mejillones Fault is not in phase with the cycle of large (Mw > 8.5) subduction earthquakes.

[57] 4. The elapsed time since the last significant earthquake (Mw 6.6) is 3.3 ± 0.3 ka.

[58] 5. The stratigraphic record of earthquakes in the trenches indicates that the seismic regime in the Mejillones Fault does not follow a characteristic behavior.

[59] According to our paleoseismological data we conclude that the reactivation of Mejillones Fault by an earthquake Mw 7.0 can rupture its entire seismogenic zone. If this fault is a good proxy for other faults of the area, seismic energy production at this active continental margin is not only related to the interplate dynamics, but also to seismic processes in the upper plate.

[60] **Acknowledgments.** We thank the Chilean National Science Foundation (FONDECYT) for the financial support of our research through the grant FONDECYT 1085117 to G.G.L. J.C.A. is supported by a PhD scholarship from CONICYT Chile. We acknowledge the logistical support of Universidad Católica del Norte. We thank the Editor, Todd Ehlers; the Associate Editor, Eric Kirby; and reviewers Daniel Melnick and Sinan Akciz for their constructive and useful corrections and suggestions. We appreciate the assistance of Rodrigo Riquelme and Cristian Toledo in our field work. We thank also Sebastien Carretier, Dominique Chardon, and Joseph Martinod for discussions during the preparation of the manuscript. Finally, we thank Elaine McDougall for her assistance with the cosmogenic ^{10}Be sample preparation and Georgina King and Ross Somerville for laboratory assistance with the OSL dating.

References

Allmendinger, R. W., and G. González (2010), Neogene to Quaternary tectonics of the coastal Cordillera, northern Chile, *Tectonophysics*, *495*(1–2), 93–110, doi:10.1016/j.tecto.2009.04.019.

Allmendinger, R. W., G. González, J. Yu, G. Hoke, and B. Isacks (2005), Trench-parallel shortening in the northern Chilean forearc: Tectonic and climatic implications, *Geol. Soc. Am. Bull.*, *117*(1), 89–104, doi:10.1130/B25505.1.

Anderson, R., J. Repka, and G. Dick (1996), Explicit treatment of inheritance in dating depositional surfaces using in situ ^{10}Be and ^{26}Al, *Geology*, *24*, 47–51, doi:10.1130/0091-7613(1996)024<0047:ETOIID>2.3.CO;2.

Angermann, D., J. Klotz, and C. Reigber (1999), Space- geodetic estimation of the Nazca- South America Euler vector, *Earth Planet. Sci. Lett.*, *171*, 329–334, doi:10.1016/S0012-821X(99)00173-9.

Arabasz, W. J. (1971), Geological and geophysical studies of the Atacama Fault System in northern Chile, PhD thesis, 264 pp., Calif. Inst. of Technol., Pasadena.

Armijo, R., and R. Thiele (1990), Active faulting in northern Chile: Ramp stacking and lateral decoupling along a subduction plate boundary?, *Earth Planet. Sci. Lett.*, *98*, 40–61, doi:10.1016/0012-821X(90)90087-E.

Arriagada, C., et al. (2011), Nature and tectonic significance of co-seismic structures associated with the Mw 8.8 Maule earthquake, central-southern Chile forearc, *J. Struct. Geol.*, *33*, 891–897.

Balco, G., J. O. Stone, N. A. Lifton, and T. J. Dunai (2008), A complete and easily accessible means of calculating surface exposure ages or erosion rates from ^{10}Be and ^{26}Al measurements, *Quat. Geochronol.*, *3*, 174–195, doi:10.1016/j.quageo.2007.12.001.

Behr, W. M., et al. (2010), Uncertainties in slip-rate estimates for the Mission Creek strand of the southern San Andreas fault at Biskra Palms Oasis, southern California, *Geol. Soc. Am. Bull.*, *122*, 1360–1377, doi:10.1130/B30020.1.

Bevis, M., E. C. Kendrick, R. Smalley Jr., T. Herring, J. Godoy, and F. Galban (1999), Crustal motion north and south of the Arica deflection: Comparing recent geodetic results from the central Andes, *Geochem. Geophys. Geosyst.*, *1*(12), 1005, doi:10.1029/1999GC000011.

Brown, E., D. Bourles, B. Burchfiel, Q. Deng, J. Li, P. Molnar, G. Raisbeck, and F. Yiou (1998), Estimation of slip rates in the southern Tien Shan using cosmic ray exposure dates of abandoned alluvial fans, *Geol. Soc. Am. Bull.*, *110*(3), 377–386, doi:10.1130/0016-7606(1998)110<0377:EOSRIT>2.3.CO;2.

Buske, S., S. Lüth, H. Meyer, R. Patzig, C. Reichert, S. Shapiro, P. Wigger, and M. Yoon (2002), Broad depth range seismic imaging of the subducted Nazca Slab, North Chile, *Tectonophysics*, *350*, 273–282, doi:10.1016/S0040-1951(02)00117-8.

Carrizo, D., G. González, and T. Dunai (2008), Constricción neógena en la cordillera de la costa norte de Chile: Neotectónica y datación de superficies con ^{21}Ne cosmogénico, *Rev. Geol. Chile*, *35*(1), 1–38, doi:10.4067/S0716-02082008000100001.

Chlieh, M., J. de Chabalier, J. Ruegg, R. Armijo, R. Dmowska, J. Campos, and K. Feigl (2004), Crustal deformation and fault slip during the seismic cycle in the North Chile subduction zone, from GPS and InSAR observations, *Geophys. J. Int.*, *158*, 695–711, doi:10.1111/j.1365-246X.2004.02326.x.

Comte, D., and M. Pardo (1991), Reappraisal of great historical earthquakes in the northern Chile and southern Peru seismic gaps, *Nat. Hazards*, *4*, 23–44, doi:10.1007/BF00126557.

Comte, D., M. Pardo, L. Dorbath, C. Dorbath, H. Haessler, L. Rivera, A. Cisternas, and L. Ponce (1992), Crustal seismicity and subduction

morphology around Antofagasta, Chile: Preliminary results from a microearthquake survey, *Tectonophysics*, *205*, 13–22, doi:10.1016/0040-1951(92)90414-2.

Comte, D., M. Pardo, L. Dorbath, C. Dorbath, H. Haessler, L. Rivera, A. Cisternas, and L. Ponce (1994), Determination of seismogenic interplate contact zone and crustal seismicity around Antofagasta, northern Chile using local data, *Geophys. J. Int.*, *116*, 553–561, doi:10.1111/j.1365-246X.1994.tb03279.x.

Comte, D., L. Dorbath, M. Pardo, T. Monfret, H. Haessler, L. Rivera, M. Frogneux, B. Glass, and C. Meneses (1999), A double-layered seismic zone in Arica, northern Chile, *Geophys. Res. Lett.*, *26*, 1965–1968, doi:10.1029/1999GL900447.

Comte, D., M. Farías, S. Roecker, D. Carrizo, and M. Pardo (2010), Crustal normal faulting triggered by the Mw=8.8 Maule megathrust subduction earthquake in central Chile, Abstract G33A-0816 presented at 2010 Fall Meeting, AGU, San Francisco, Calif., 13–17 Dec.

Delouis, B., A. Cisternas, L. Dorbath, L. Rivera, and E. Kausel (1996), The Andean subduction zone between 22°S and 24°S (northern Chile): Precise geometry and state of stress, *Tectonophysics*, *259*, 81–100, doi:10.1016/0040-1951(95)00065-8.

Delouis, B., et al. (1997), The Mw=8.0 Antofagasta (northern Chile) Earthquake of 30 July 1995: A Precursor to the End of the Large 1877 Gap, *Bull. Seismol. Soc. Am.*, *87*(2), 427–445.

Delouis, B., H. Philip, L. Dorbath, and A. Cisternas (1998), Recent crustal deformation in the Antofagasta Region (northern Chile) and the subduction process, *Geophys. J. Int.*, *132*, 302–338, doi:10.1046/j.1365-246x.1998.00439.x.

Delouis, B., M. Pardo, D. Legrand, and T. Monfret (2009), The Mw 7.7 Tocopilla earthquake of 14 November 2007 at the southern edge of the northern Chile seismic gap: Rupture in the deep part of the coupled plate interface, *Bull. Seismol. Soc. Am.*, *99*(1), 87, doi:10.1785/0120080192.

Dunai, T. J. (2000), Scaling factors for production rates of in-situ produced cosmogenic nuclides: A critical reevaluation, *Earth Planet. Sci. Lett.*, *176*, 157–169, doi:10.1016/S0012-821X(99)00310-6.

Galbraith, R. F., R. G. Roberts, G. M. Laslett, H. Yoshida, and J. M. Olley (1999), Optical dating of single and multiple grains of quartz from Jinmium rock shelter, northern Australia: Part I, Experimental design and statistical models, *Archaeometry*, *41*, 339–364, doi:10.1111/j.1475-4754.1999.tb00987.x.

González, G., J. Cembrano, D. Carrizo, A. Macci, and H. Schneider (2003), The link between forearc tectonics and Pliocene–Quaternary deformation of the Coastal Cordillera, northern Chile, *J. South Am. Earth Sci.*, *16*, 321–342, doi:10.1016/S0895-9811(03)00100-7.

González, J., G. Vargas, and G. González (2009), Antecedentes preliminares de reconocimiento de fallas submarinas en la Península de Mejillones, 22°45′–23°05′ S, abstract S9_033 presented at XII Congreso Geológico Chileno, Univ. de Chile, Santiago, 22–26 Nov.

Granger, D. E., and A. L. Smith (2000), Dating buried sediments using radioactive decay and muogenic production of ^{26}Aland ^{10}Be, *Nucl. Instrum. Methods Phys. Res., Sect. B*, *172*, 822–826, doi:10.1016/S0168-583X(00)00087-2.

Husen, S., E. Kissling, E. Flueh, and G. Asch (1999), Accurate hypocentre determination in the seismogenic zone of the subducting Nazca Plate in northern Chile using a combined on/offshore network, *Geophys. J. Int.*, *138*(3), 687–701, doi:10.1046/j.1365-246x.1999.00893.x.

Husen, S., E. Kissling, and E. Flueh (2000), Local earthquake tomography of shallow subduction in North Chile: A combined onshore and offshore study, *J. Geophys. Res.*, *105*, 28,183–28,198, doi:10.1029/2000JB900229.

Kanamori, H. (1977), The energy release in great earthquakes, *J. Geophys. Res.*, *82*, 2981–2987, doi:10.1029/JB082i020p02981.

Klotz, J., G. Michel, G. Khazaradze, and B. Heinze (2001), GPS based deformation measurements and modeling, in Deformation Processes in the Andes, Project D5, *Rep. SBF 267*, pp. 361–394, GFZ Potsdam, Potsdam, Germany.

Klotz, J., A. Abolghasem, G. Khazaradze, B. Heinze, T. Victor, R. Hackney, K. Bataille, R. Maturana, J. Viramonte, and R. Perdomo (2006), Long-term signals in the present-day deformation field of the Central Andes and Southern Andes and constraint on the viscosity of the Earth's upper mantle, in *The Andes Active Subduction Orogeny*, edited by O. Oncken et al., pp. 65–90, Springer, Berlin.

Kober, F., S. Ivy-Ochs, F. Schlunegger, H. Baur, P. W. Kubik, and R. Wieler (2007), Denudation rates and a topography-driven rainfall threshold in northern Chile: Multiple cosmogenic nuclide data and sediment yield budgets, *Geomorphology*, *83*(1–2), 97–120, doi:10.1016/j.geomorph.2006.06.029.

Lal, D. (1991), Cosmic ray labeling of erosion surfaces: *In situ* nuclide production rates and erosion rates and erosion models, *Earth Planet. Sci. Lett.*, *104*, 424–439, doi:10.1016/0012-821X(91)90220-C.

Loveless, J. P., G. D. Hoke, R. W. Allmendinger, G. González, B. L. Isacks, and D. A. Carrizo (2005), Pervasive cracking of the northern Chilean Coastal Cordillera: New evidence for forearc extension, *Geology*, *33*(12), 973–976, doi:10.1130/G22004.1.

Marquardt, C. (2005), Déformations Néogènes le long de la Côte Nord du Chili (23°–27° S), Avant-Arc des Andes Centrales, PhD thesis, 212 pp., Lab. des Mec. et Tranferts en Geol., Univ. Toulouse III-Paul Sabatier, Toulouse, France.

Marquardt, C., A. Lavenu, L. Ortlieb, E. Godoy, and D. Comte (2004), Coastal neotectonics in Southern Central Andes: Uplift and deformation of marine terraces in Northern Chile (27°S), *Tectonophysics*, *394*, 193–219, doi:10.1016/j.tecto.2004.07.059.

Mason, D. B. (1992), Earthquake magnitude potential of active faults in the Intermountain Seismic Belt from surface parameter scaling, MS thesis, 110 pp., Univ. of Utah, Salt Lake City.

Matmon, A., D. P. Schwartz, R. Finkel, S. Clemmens, and T. Hanks (2005), Dating offset fans along the Mojave section of the San Andreas fault using cosmogenic ^{26}Al and ^{10}Be, *Geol. Soc. Am. Bull.*, *117*, 795–807, doi:10.1130/B25590.1.

McCalpin, J. (1996), *Paleoseismology*, 588 pp., Academic, San Diego, Calif.

Motagh, M., B. Schurr, J. Anderssohn, B. Cailleau, T. Walter, R. Wang, and J. Villotte (2010), Subduction earthquake deformation associated with 14 November 2007, Mw 7.8. Tocopilla earthquake in Chile: Results from InSAR and aftershocks, *Tectonophysics*, *490*, 60–68, doi:10.1016/j.tecto.2010.04.033.

Nelson, A. R. (1992), Lithofacies analysis of colluvial sediments—An aid in interpreting the recent history of Quaternary normal faults in the Basin and Range province, western United States, *J. Sediment. Petrol.*, *62*, 607–621.

Niemeyer, H., G. González, and E. Martínez-De los Ríos (1996), Evolución tectónica cenozoica del margen continental activo de Antofagasta, norte de Chile, *Rev. Geol. Chile*, *23*(2), 165–186.

Nishenko, S. P. (1991), Circum-Pacific seismic potential, 1989–1999, *Pure Appl. Geophys.*, *135*, 169–259, doi:10.1007/BF00880240.

Okada, A. (1971), On the tectonics of the Atacama fault zone region-preliminary notes on Late Cenozoic faulting and geomorphic development of the Coastal Range of Northern Chile, *Bull. Dep. Geogr. Univ. Tokyo*, *3*, 47–65.

Ortlieb, L., N. Guzman, and C. Marquardt (2003), A longer lasting and warmer interglacial episode during isotopic stage 11: Marine terrace evidence in tropical Western Americas, in *Earth's Climate and Orbital Eccentricity: The Marine Isotope Stage 11*, *Geophys. Monogr. Ser.*, vol. 137, edited by A. Droxler, R. Z. Poore, and L. H. Burkle, pp. 157–180, AGU, doi:10.1029/137GM12.

Pelz, K. (2000), Tektonische Erosion am zentralandinen Forearc (20°–24° S), *Sci. Tech. Rep. 00/20*, 118 pp., GFZ Potsdam, Potsdam, Germany.

Placzek, C., A. Matmon, D. Granger, J. Quade, and S. Niedermann (2010), Evidence for active landscape evolution in the hyperarid atacama from multiple terrestrial cosmogenic nuclides, *Earth Planet. Sci. Lett.*, *295*(1–2), 12–20, doi:10.1016/j.epsl.2010.03.006.

Prescott, J. R., and J. T. Hutton (1994), Cosmic ray contributions to dose rates for luminescence and ESR dating: large depths and long-term time variations, *Radiat. Meas.*, *23*, 497–500, doi:10.1016/1350-4487(94)90086-8.

Putkonen, J., and T. Swanson (2003), Accuracy of cosmogenic ages for moraines, *Quat. Res.*, *59*(2), 255–261, doi:10.1016/S0033-5894(03)00006-1.

Quezada, J. (2006), Interacción entre procesos tectónicos y procesos erosivos en la configuración del relieve litoral del Norte de Chile, PhD thesis, Univ. Católica del Norte, Antofagasta, Chile.

Repka, J. L., R. S. Anderson, and R. C. Finkel (1997), Cosmogenic dating of fluvial terraces, Fremont River, Utah, *Earth Planet. Sci. Lett.*, *152*, 59–73, doi:10.1016/S0012-821X(97)00149-0.

Rodnight, H., G. A. T. Duller, A. G. Wintle, and S. Tooth (2006), Assessing the reproducibility and accuracy of optical dating of fluvial deposits, *Quat. Geochronol.*, *1*, 109–120, doi:10.1016/j.quageo.2006.05.017.

Shackleton, N. J., A. Berger, and W. R. Peltier (1990), An alternative astronomical calibration of the lower Pleistocene time scale based on ODP site 677: *Royal Society of Edinburgh Transactions*, *Earth Sci.*, *81*, 251–261.

Slemmons, B. D., and C. Depolo (1986), Evaluation of Active Faulting and Associated Hazards, in *Active Tectonics*, pp. 45–62, Natl. Acad. Press, Washington, D. C.

Springer, M., and A. Forster (1998), Heat-flow density across the Central Andean subduction zone, *Tectonophysics*, *291*, 123–139, doi:10.1016/S0040-1951(98)00035-3.

Tichelaar, B., and L. Ruff (1991), Seismic Coupling Along the Chilean Subduction Zone, *J. Geophys. Res.*, *96*(B7), 11,997–12,022, doi:10.1029/91JB00200.

Vargas, G., L. Ortlieb, and J. Rutllant (2000), Aluviones históricos en Antofagasta y su relación con eventos El Niño/Oscilación del Sur, *Rev. Geol. Chile*, *27*, 157–176.

Vargas, G., J. Rutllant, and L. Ortlieb (2006), ENSO tropical–extratropical climate teleconnections and mechanisms for Holocene debris flows along the hyperarid coast of western South America (17°–24°S), *Earth Planet. Sci. Lett.*, *249*, 467–483, doi:10.1016/j.epsl.2006.07.022.

Vargas, G., C. Palacios, M. Reich, S. Luo, C. Shen, and G. González (2011), U-series dating of co-seismic gypsum and submarine paleoseismology of active faults in Northern Chile (23°S), *Tectonophysics*, *497*, 34–44, doi:10.1016/j.tecto.2010.10.017.

Victor, P., M. Sobiesiak, J. Glodny, S. N. Nielsen, and O. Oncken (2011), Long-term persistence of subduction earthquake segment boundaries: Evidence from Mejillones Peninsula, northern Chile, *J. Geophys. Res.*, *116*, B02402, doi:10.1029/2010JB007771.

Wallace, R. E. (1977), Profiles and ages of young fault scarps, north-central Nevada, *Geol. Soc. Am. Bull.*, *88*, 1267–1281, doi:10.1130/0016-7606(1977)88<1267:PAAOYF>2.0.CO;2.

Wells, D. L., and K. J. Coppersmith (1994), New empirical relationships among magnitude, rupture length, rupture width, rupture area, and surface displacement, *Bull. Seismol. Soc. Am.*, *84*, 974–1002.

Wesnousky, S. (2008), Displacement and geometrical characteristics of earthquake surface ruptures: Issues and implications for seismic-hazard analysis and the process of earthquake rupture, *Bull. Seismol. Soc. Am.*, *98*, 1609–1632, doi:10.1785/0120070111.

Wintle, A. G., and A. S. Murray (2006), A review of quartz optically stimulated luminescence characteristics and their relevance in single-aliquot regeneration dating protocols, *Radiat. Meas.*, *41*, 369–391, doi:10.1016/j.radmeas.2005.11.001.

S. A. Binnie, Institut für Geologie und Mineralogie, Universität zu Köln, Zülpicher Str. 49b, D-50674 Köln, Germany.

J. A. Cortés and G. L. González, Departamento de Ciencias Geológicas, Universidad Católica del Norte, Avenida Angamos 0610, Antofagasta, Chile. (jcortesa@ucn.cl)

S. P. H. T. Freeman, Scottish Universities Environmental Research Centre, Rankine Avenue, Scottish Enterprise Technology Park, East Kilbride G75 0QF, UK.

R. Robinson, Department of Earth Sciences, University of St Andrews, St Andrews KY16 9AL, UK.

G. E. Vargas, Departamento de Geología, Facultad de Ciencias Físicas y Matemáticas, Universidad de Chile, Santiago 8320000, Chile.